nature electronics

SUPPLEMENTARY INFORMATION

https://doi.org/10.1038/s41928-018-0189-7

In the format provided by the authors and unedited.

Three-dimensional piezoelectric polymer microsystems for vibrational energy harvesting, robotic interfaces and biomedical implants

Mengdi Han[1,14], Heling Wang[2,3,4,14], Yiyuan Yang[3], Cunman Liang[1,5], Wubin Bai[1,2], Zheng Yan[6], Haibo Li[4,7], Yeguang Xue[2,3,4], Xinlong Wang[8], Banu Akar[8], Hangbo Zhao[1], Haiwen Luan[2,3,4], Jaeman Lim[1], Irawati Kandela[9], Guillermo A. Ameer[8,10,11], Yihui Zhang[12]*, Yonggang Huang[1,2,3,4]* and John A. Rogers[1,2,3,8,11,13]*

[1]Center for Bio-Integrated Electronics, Northwestern University, Evanston, IL, USA. [2]Department of Materials Science and Engineering, Northwestern University, Evanston, IL, USA. [3]Department of Mechanical Engineering, Northwestern University, Evanston, IL, USA. [4]Departments of Civil and Environmental Engineering, Northwestern University, Evanston, IL, USA. [5]Key Laboratory of Mechanism Theory and Equipment Design of Ministry of Education, School of Mechanical Engineering, Tianjin University, Tianjin, China. [6]Departments of Biomedical, Biological & Chemical Engineering, Mechanical and Aerospace Engineering, University of Missouri, Columbia, MO, USA. [7]School of Naval Architecture, Ocean and Civil Engineering (State Key Laboratory of Ocean Engineering), Shanghai Jiaotong University, Shanghai, China. [8]Department of Biomedical Engineering, Northwestern University, Evanston, IL, USA. [9]The Center for Developmental Therapeutics, Northwestern University, Evanston, IL, USA. [10]Department of Surgery at Northwestern University Feinberg School of Medicine, Chicago, IL, USA. [11]Center for Advanced Regenerative Engineering, Northwestern University, Evanston, IL, USA. [12]Center for Flexible Electronics Technology and Center for Mechanics and Materials; AML, Department of Engineering Mechanics, Tsinghua University, Beijing, China. [13]Departments of Neurological Surgery, Chemistry, Electrical Engineering and Computer Science; and Simpson Querrey Institute for BioNanotechnology, Northwestern University, Evanston, IL, USA. [14]These authors contributed equally: Mengdi Han, Heling Wang. *e-mail: yihuizhang@tsinghua.edu.cn; y-huang@northwestern.edu; jrogers@northwestern.edu

Supplementary Note 1: Representative step-by-step fabrication procedures for 3D piezoelectric microsystems

Preparing substrates

1. Clean PVDF film (28 μm in thickness) with IPA

2. Deposit Cr/Au (5 nm/50 nm in thickness) on both sides of PVDF film

3. Clean silicon wafer (500 μm in thickness) with acetone and IPA

4. Spin coat PDMS (1:10) at 3000 rpm on silicon wafer

5. Bake at 70 ˚C for 1 h

6. Transfer PVDF film onto PDMS-coated silicon wafer

Defining 2D patterns

7. Define 2D pattern with photoresist (AZ 5214)

8. Wet etch Au and Cr with commercial etchants

9. Dry etch PVDF through RIE (220 mTorr, 25 sccm O_2, RF power of 200 W for 120 min)

Defining creases

10. Define creases with photoresist (AZ 5214)

11. Wet etch Au and Cr with commercial etchants

12. Dry etch PVDF through RIE (220 mTorr, 25 sccm O_2, RF power of 200 W for 90 min). Controlling the etching time yields creases with different thicknesses.

Defining top electrode

13. Define top electrode with photoresist (AZ 4620)

14. Wet etch Au and Cr with commercial etchants

Defining bottom electrode

15. Transfer PVDF film to PVA tape

16. Laminate PVA tape onto another PDMS-coated silicon wafer, with PVDF side facing up

17. Clamp the sample and dissolve PVA tape with warm water

18. Define bottom electrode with photoresist (AZ 4620)

19. Wet etch Au and Cr with commercial etchants

Transfer printing

20. Transfer PVDF film to PVA tape

21. Laminate PVA tape onto another PDMS-coated silicon wafer, with PVDF side facing up

22. Clamp the sample and dissolve PVA tape with warm water

23. Transfer PVDF film to PVA tape again (to flip the top and bottom sides)

24. Deposit Ti/SiO_2 (10 nm/100 nm in thickness) through shadow mask to define the bonding sites

Compressive buckling

25. UVO treatment of silicone elastomer (Dragon Skin, 700 μm in thickness) and PVDF 2D precursors for 5 min

26. Transfer print PVDF 2D precursors onto stretched silicone elastomer

27. Heat the samples in the oven at 70 ˚C for 10 min

28. Dissolve PVA tape with warm water

29. Release stretched silicone elastomer to form 3D PVDF mesostructures

Supplementary Note 2: Finite element analysis (FEA) and calculation of output voltage

Shape, deformation and vibration of 3D structures

FEA was adopted to predict the 2D-to-3D shape transformation induced by the compressive strain, the deformation of the 3D structure under applied force and the vibration driven by a vibrational platform. FEA was conducted by the commercial software ABAQUS (version 6.14, standard). To overcome the energy barrier that prevented the 2D-to-3D shape transformation, an initial geometric imperfection was introduced such that the 2D precursor evolved to the accurate 3D shape under compressive strain. For those structures with ultra-low stiffness serpentine pattern, the initial geometric imperfection was introduced only into the temporary supporting layer that assisted the buckling via contact. Eight-node solid element modeled the

underlying elastomeric substrate (D-skin), with the Mooney-Rivlin constitutive relationship. Eight-node solid element also modeled the added copper mass (Cu) with the linear elastic constitutive relationship. Four-node finite-strain shell element modeled the precursor, with the linear elastic constitutive relationship. The precursor consisted of piezoelectric material PVDF, metal electrodes (Au, Cr and Ti) and supporting layer (PI). The material properties (Young's modulus E, Poisson's ratio ν and density ρ) are $E_{\text{Substrate}}$=166 kPa, $\nu_{\text{Substrate}}$=0.49, $\rho_{\text{Substrate}}$=1070 kg/m^3, E_{Cu}=128 kPa, ν_{Cu}=0.36, ρ_{Cu}=8960 kg/m^3, E_{PVDF}=2 GPa, ν_{PVDF}=0.39, ρ_{PVDF}=1800 kg/m^3, E_{Au}=78 GPa, ν_{Au}=0.44, ρ_{Au}=19320 kg/m^3, E_{Cr}=279 GP, ν_{Cr}=0.21, ρ_{Cr}=7190 kg/m^3, E_{Ti}=110 GPa, ν_{Ti}=0.32, ρ_{Ti}=4506 kg/m^3, E_{PI}=2.5 GPa, ν_{PI}=0.34 and ρ_{PI}=1420 kg/m^3.

Calculation of output voltage

The open-circuit output voltage during vibration was calculated from the piezoelectric constitutive relationship and the membrane strain obtained by FEA. Assuming that the PVDF was polarized along its thickness direction (3- direction), its constitutive relationship was

$$D_3 = e_{31}\varepsilon_{11} + e_{31}\varepsilon_{22} + k_{33}E_3\,, \tag{S1}$$

where ε_{11} and ε_{22} were the strains, E_3 was the electrical field, D_3 was the electrical displacement, e_{31} =–0.03 N/(V·m) was the piezoelectric constant and k_{33}=8.85×10^{-11} F/m was the dielectric constant. The normal strain along 3- direction was neglected. Under the open-circuit condition

$$\int_{-h_{\text{PVDF}}/2}^{h_{\text{PVDF}}/2} D_3 \mathrm{d}z = 0\,, \tag{S2}$$

the open-circuit output voltage at point (x, y) was

$$v_{\text{open-circuit}}(x,y) = \int_{-h_{\text{PVDF}}/2}^{h_{\text{PVDF}}/2} E_3 \mathrm{d}z = -\frac{e_{31}h_{\text{PVDF}}}{k_{33}}\left[\varepsilon_{11(\text{m})}(x,y) + \varepsilon_{22(\text{m})}(x,y)\right], \tag{S3}$$

where h_{PVDF} was the PVDF thickness, $\varepsilon_{11(\text{m})}$ and $\varepsilon_{22(\text{m})}$ were the membrane strains in PVDF obtained by FEA. The net output voltage was the average of $v_{\text{open-circuit}}(x,y)$ over the region Ω with the electrode

$$V_{\text{open-circult}} = \frac{1}{A_\Omega}\int_\Omega v_{\text{open-circuit}}(x,y)\,\mathrm{d}x\mathrm{d}y\,, \tag{S4}$$

where A_Ω is the area of Ω. In the actual experiment condition, the voltage had to be measured in a circuit with finite resistance R. Therefore, the open-circuit condition Eq. (S2) should be replaced by [Ref. 1]

$$\frac{V}{R} = -A_{\Omega}\frac{\mathrm{d}D_3}{\mathrm{d}t}, \tag{S5}$$

which lead to

$$\frac{\mathrm{d}V}{\mathrm{d}t} + \frac{h_{\mathrm{PVDF}}}{A_{\Omega}Rk_{33}} = -\frac{e_{31}h_{\mathrm{PVDF}}}{k_{33}}\left(\frac{\mathrm{d}\varepsilon_{11(\mathrm{m})}}{\mathrm{d}t} + \frac{\mathrm{d}\varepsilon_{22(\mathrm{m})}}{\mathrm{d}t}\right), \tag{S6}$$

where V was the output voltage. Under the initial condition that V=0 at t=0, the output voltage was

$$V = -\frac{e_{31}h_{\mathrm{PVDF}}}{k_{33}}e^{-\frac{h_{\mathrm{PVDF}}}{A_{\Omega}Rk_{33}}}\int_0^t\left(\frac{\mathrm{d}\varepsilon_{11(\mathrm{m})}}{\mathrm{d}s} + \frac{\mathrm{d}\varepsilon_{22(\mathrm{m})}}{\mathrm{d}s}\right)e^{\frac{h_{\mathrm{PVDF}}s}{A_{\Omega}Rk_{33}}}\mathrm{d}s, \tag{S7}$$

Supplementary Note 3: A numerical example of the energetic analysis on buckling process

A numerical example is presented in this supplementary note to demonstrate that the serpentine pattern could not delaminate from the substrate to buckle without the temporary supporting layer but could remain in the buckle-up state after removing the supporting layer. A representative 2D precursor with serpentine pattern is shown in Supplementary Fig. 10a. Supplementary Fig. 10b and Supplementary Fig. 10c show its local buckling state and global buckling state respectively. The total energy W of the two states are compared in Supplementary Fig. 10d. The total energy consists of the strain energy and the adhesion energy $W_{\mathrm{Adhesion}} = \gamma A_{\mathrm{Adhesion}}$, where γ is the work of adhesion and A_{Adhesion} is the area of the serpentine pattern bonded to the substrate. γ is assumed to be 0.16 N/m [Ref. 2] in this analysis. FEA result shown in Supplementary Fig. 10d indicates that the local buckling state has a lower energy than the global buckling state. Therefore, without the supporting layer the serpentine pattern tends to adhere to the substrate. However, as shown by Supplementary Fig. 10e, the global buckling state is a local energy minimum such that the serpentine pattern can remain in this state after removing the supporting layer which assists the serpentine pattern to buckle-up.

FEA results in Supplementary Fig. 11b show that the structure in Fig. 2e must overcome an energy barrier of 5.5 nJ to switch from the buckle up state to the buckle down state. Assuming that all of the serpentine ribbon attaches to the PI supporting layer, the adhesion energy is estimated as ~28 nJ (serpentine area is calculated as 0.35 mm^2; the work of adhesion between PI and electrode is 0.08 $\mathrm{J/m}^2$ [Ref. 3]). However, optical images in experiment show that only a small part of the serpentine ribbon attaches to the supporting layer when the structure buckles up (Supplementary Fig. 8a). Therefore, the adhesion energy becomes much smaller and is insufficient to overcome the energy barrier.

Supplementary Note 4: Validation of the scaling laws

FEA Validations of the scaling laws presented in the manuscript are presented in this Supplementary note. To validate Eq. (1), FEA is conducted on the structure with serpentine pattern shown in Supplementary Fig. 28. The default geometry/material parameters are L=2.5 mm, H=1.2 mm, S=25 mm, h=9 μm, b=50 μm and E=2 GPa. One of the above parameters are changed at one time with the others fixed. FEA then obtains the displacement u vs. force F curves. After normalizing u by L and F by $\frac{Ebh^3L}{H^2S}$, the $\frac{u}{L}$ vs. $\frac{FH^2S}{Ebh^3L}$ curves are the same for various sets of parameters as shown in Supplementary Figs. 30a-f, which validates the scaling law Eq. (1). The stiffness $K=\left.\frac{\partial F}{\partial u}\right|_{u\to 0}$ is then calculated from the u vs. force F curves obtained above. As shown in Supplementary Fig. 32, the K vs. $\frac{Ebh^3}{H^2S}$ relationship falls on a straight line, which validates that K is proportional to $\frac{Ebh^3}{H^2S}$. To validate the scaling law of the resonant frequency (f) Eq. (2), with one of the three parameters (h, H, S) changed at a time, FEA prediction of the f vs. $\frac{h}{HS}\sqrt{\frac{E}{\rho}}$ relationship falls on a straight line as shown in Fig. 2l and Supplementary Fig. 33a. The coefficient α in the scaling law, i.e. the slope of the straight line in Fig. 2l, is fitted to be 0.65 by the method of least squares. The scaling law also suggests that the resonant frequency does not depend on the serpentine length L and ribbon width w. FEA results presented in Supplementary Figs. 33b and c show that the resonant frequency f changes little with L and w, which is consistent with the scaling law.

Reference:

1. Su, Y., Dagdeviren, C. & Li, R. Measured output voltages of piezoelectric devices depend on the resistance of voltmeter. *Advanced Functional Materials* **25**, 5320–5325 (2015).

2. Wang, S. et al. Mechanics of curvilinear electronics. *Soft Matter* **6**, 5757–5763 (2010).

3. Park, S. et al. Influence of surface treatment of polyimide film on adhesion enhancement between polyimide and metal films. *Bulletin of the Korean Chemical Society* **28**, 188–192 (2007).

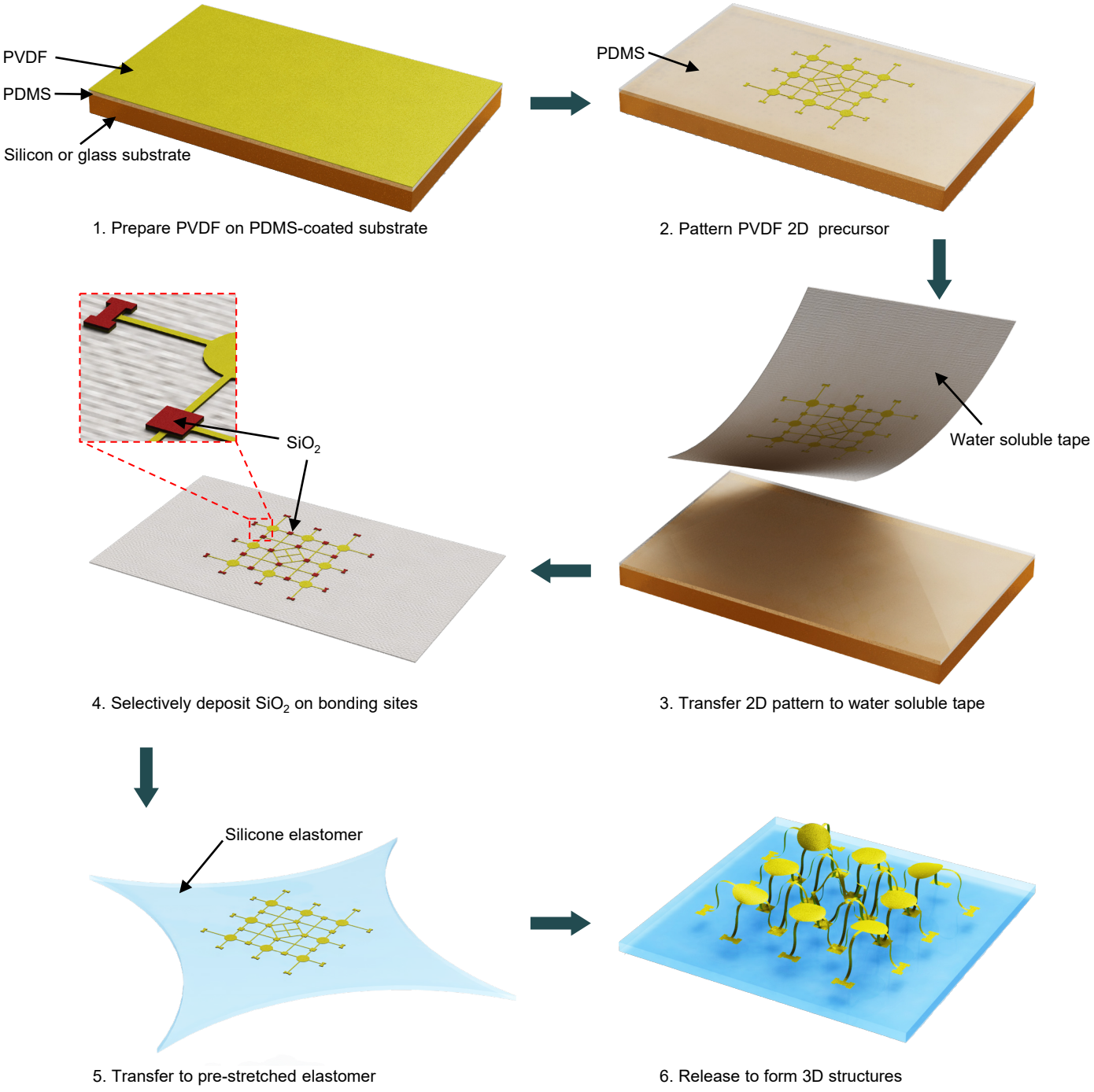

Supplementary Figure 1. Fabrication scheme for 3D piezoelectric microsystems

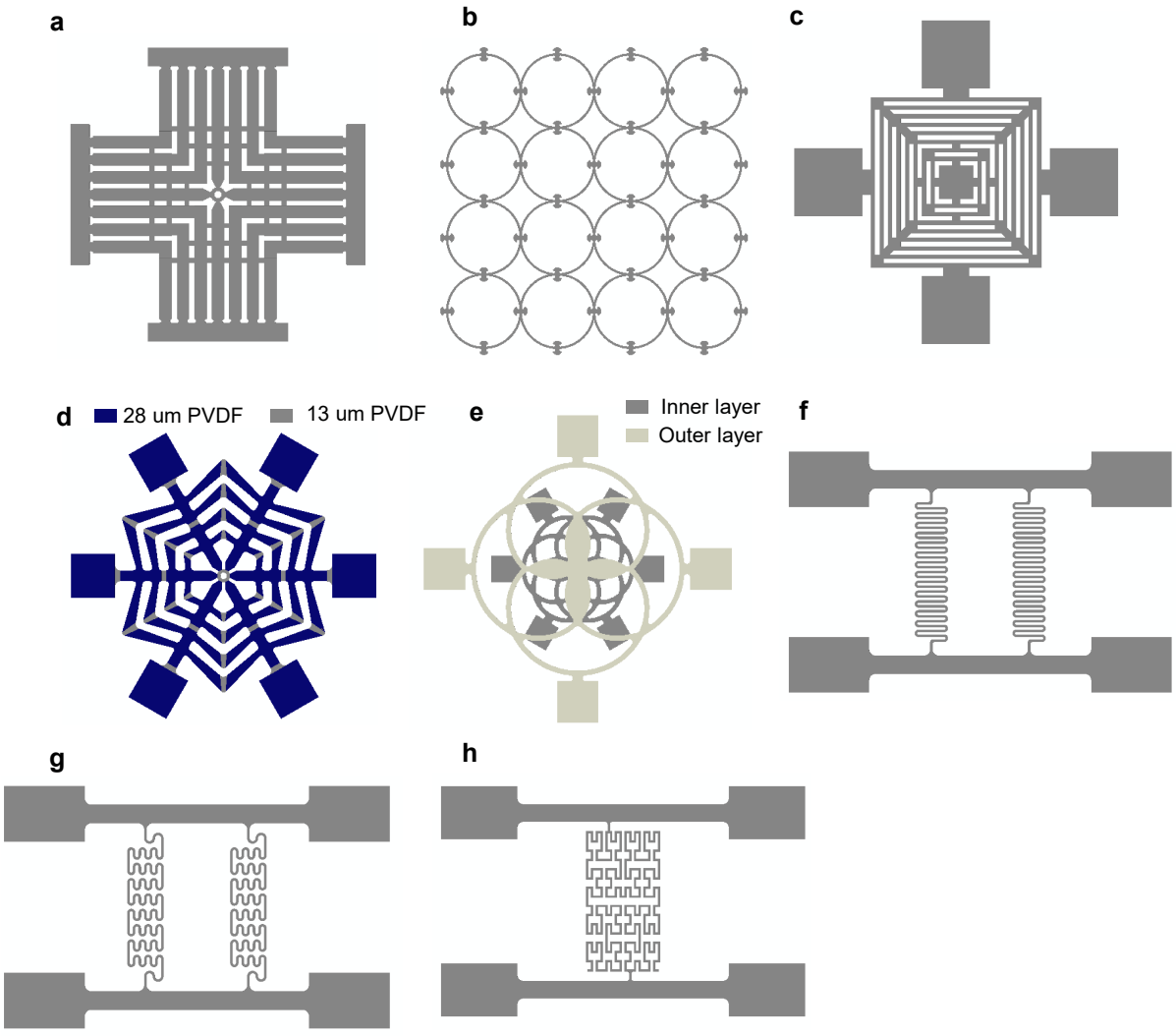

Supplementary Figure 2. Precursor of the structures shown in Fig.1.

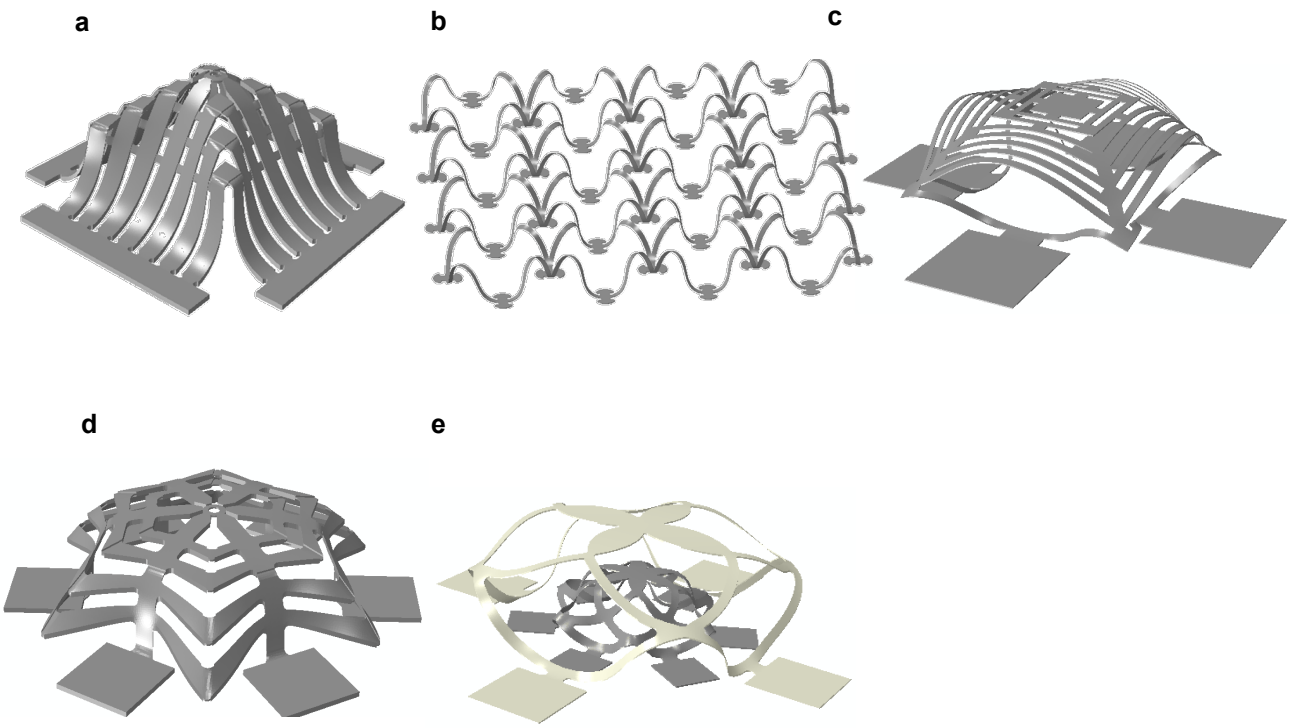

Supplementary Figure 3. FEA prediction of the buckled shape for the structures in Fig. 1a and b.

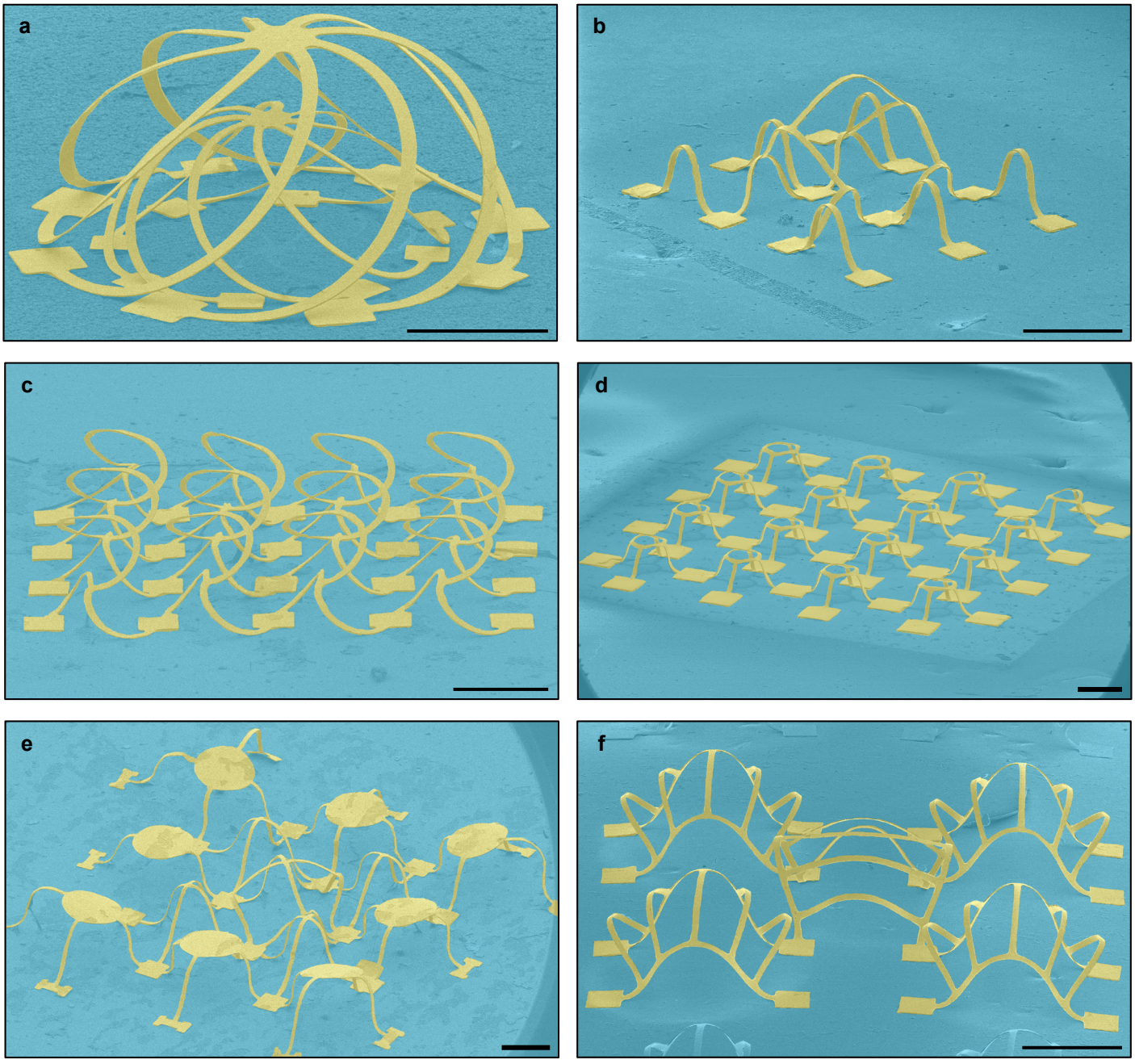

Supplementary Figure 4. SEM images of representative 3D filamentary mesostructures in PVDF. a, Bilayer cage. **b,** Triple-floor building. **c,** Double-floor network. **d,** 4 by 4 raised ring array. **e,** Table–tent mixed array. **f,** Peacock array. Scale bars, 500 μm.

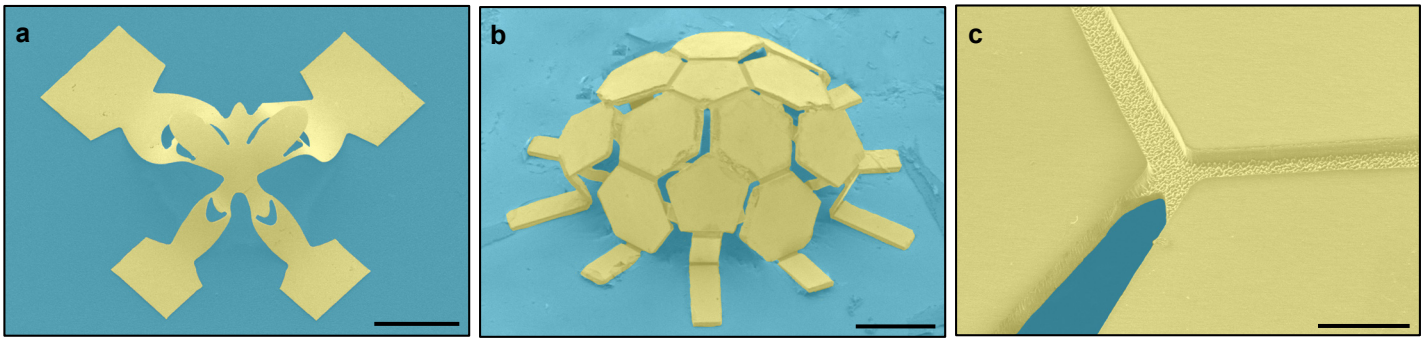

Supplementary Figure 5. SEM images of representative 3D mesostructures of membranes in PVDF. a, Kirigami-inspired butterfly. Scale bar, 500 μm. **b,** Origami-inspired football. Scale bar, 500 μm. **c,** Magnified view of the football structure. Scale bar, 100 μm.

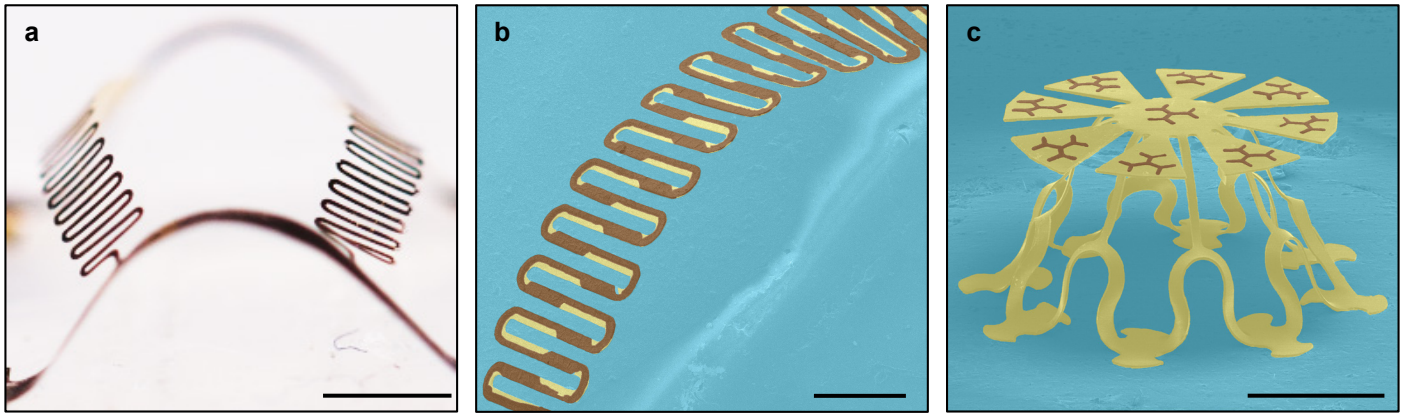

Supplementary Figure 6. 3D PVDF mesostructures with metal patterns. a, Optical image of a 3D serpentine structure. Scale bar, 2 mm. **b,** SEM image of the 3D serpentine structure with magnified view. Scale bar, 500 μm. **c,** SEM image of a jellyfish structure with metal patterns on top. Scale bar, 500 μm.

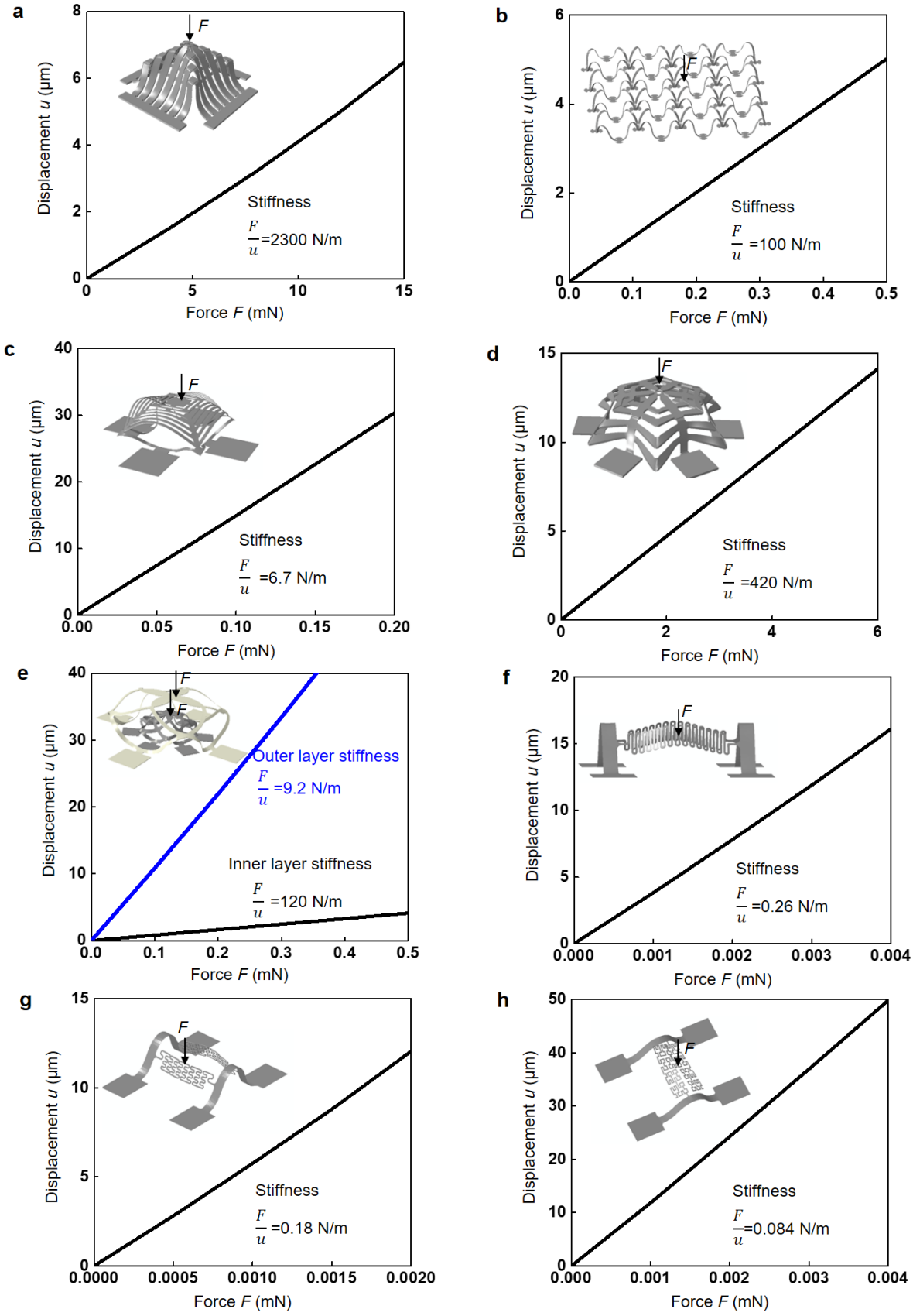

Supplementary Figure 7. FEA results of the relationship of displacement vs. force to illustrate the stiffness of the structures in Fig. 1. The stiffness of the serpentines structures (**f-g**) are at least one order of magnitude smaller than those of the conventional structures (**a-e**)

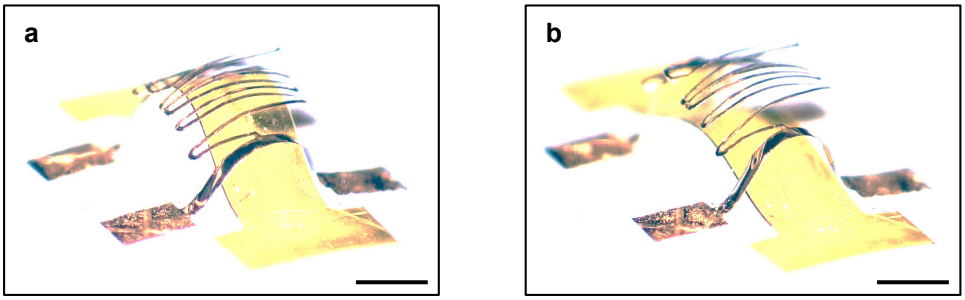

Supplementary Figure 8. Optical images of an ultra-low-stiffness 3D mesostructure. a, The ultra-low-stiffness 3D mesostructure with supporting layer. **b,** Separation of the supporting layer from the ultra-low-stiffness 3D mesostructure. Scale bars, 500 μm.

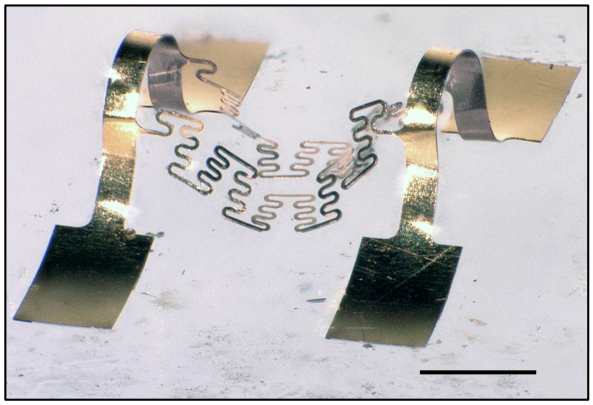

Supplementary Figure 9. Optical image of an ultra-low-stiffness serpentine buckled without temporary supporting layer. Scale bars, 500 μm.

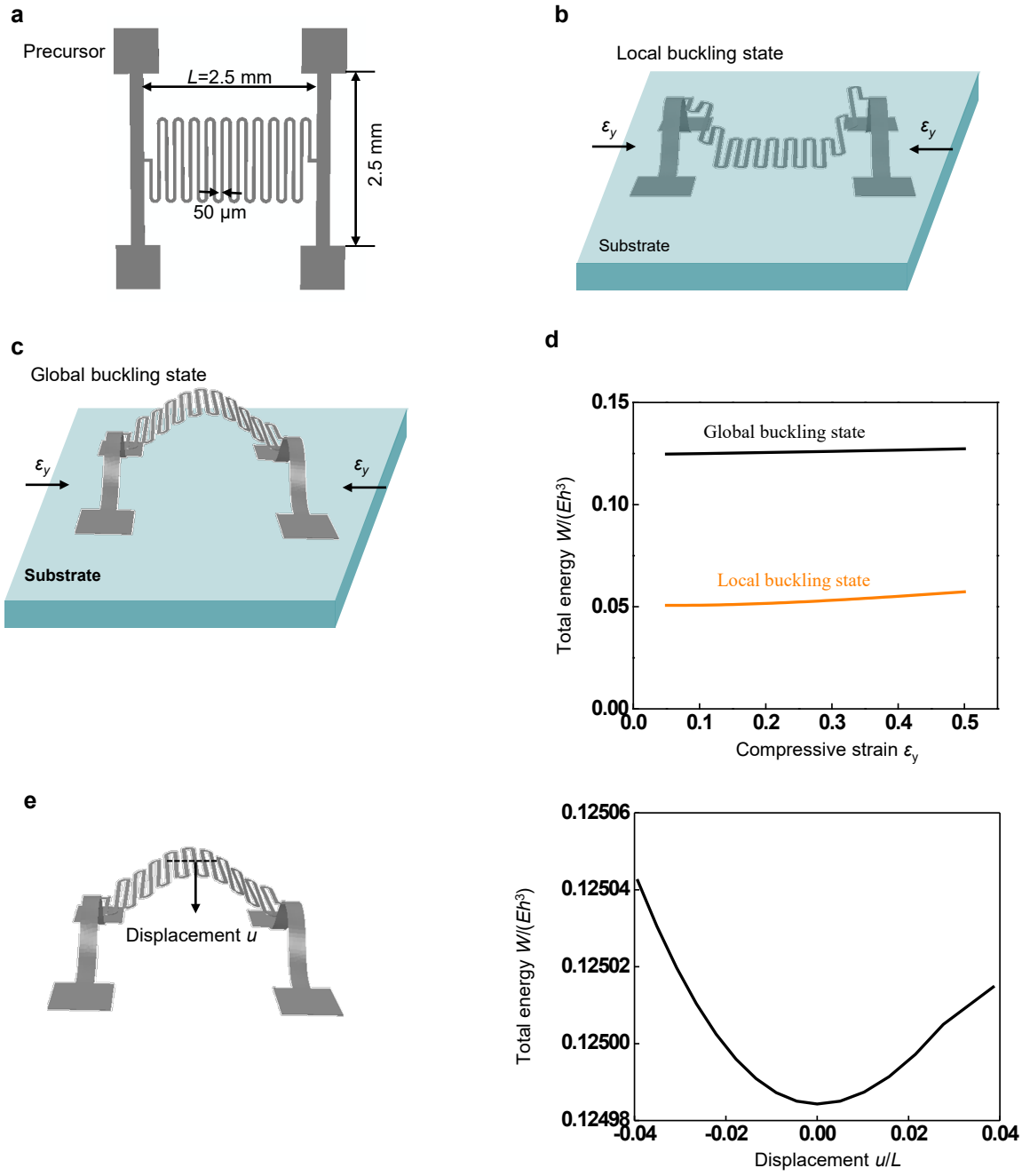

Supplementary Figure 10. A numerical example of the energetic analysis on the serpentine pattern. a, geometry of the 2D precursor. **b,** Local buckling state, in which the serpentine adheres to the substrate. **c,** Global buckling state, in which the serpentine buckles up. **d,** Total energy of the two states. **e,** Total energy vs. serpentine displacement measured from the global buckling state.

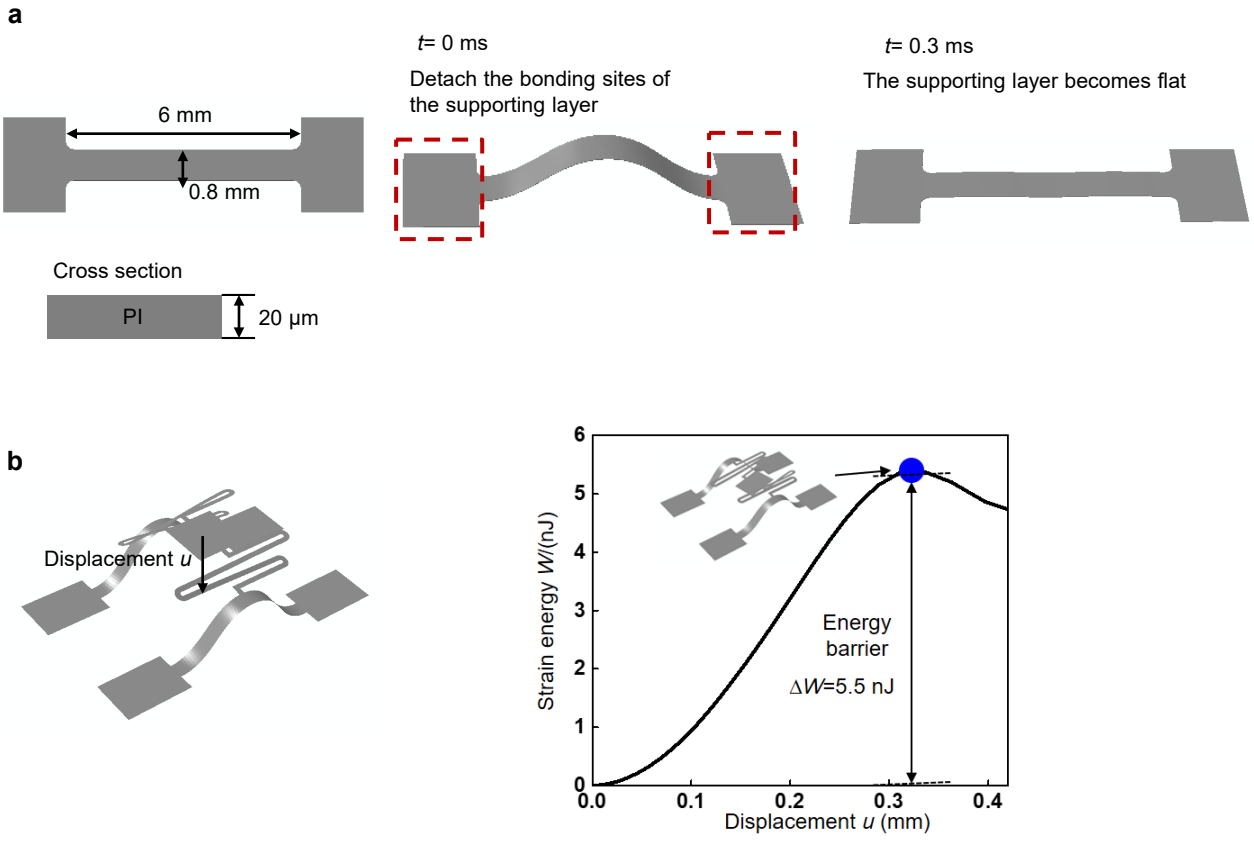

Supplementary Figure 11. a, FEA illustration of the deformation of the supporting layer after release from its bonding site**.** left frame: geometry of the 2D precursor; middle frame: at *t*=0 ms, release the bonding site; right frame: after 0.3 ms the supporting layer becomes flat. **b**. strain energy vs. serpentine displacement for the structure in Fig. 2e when it is pressed downwards.

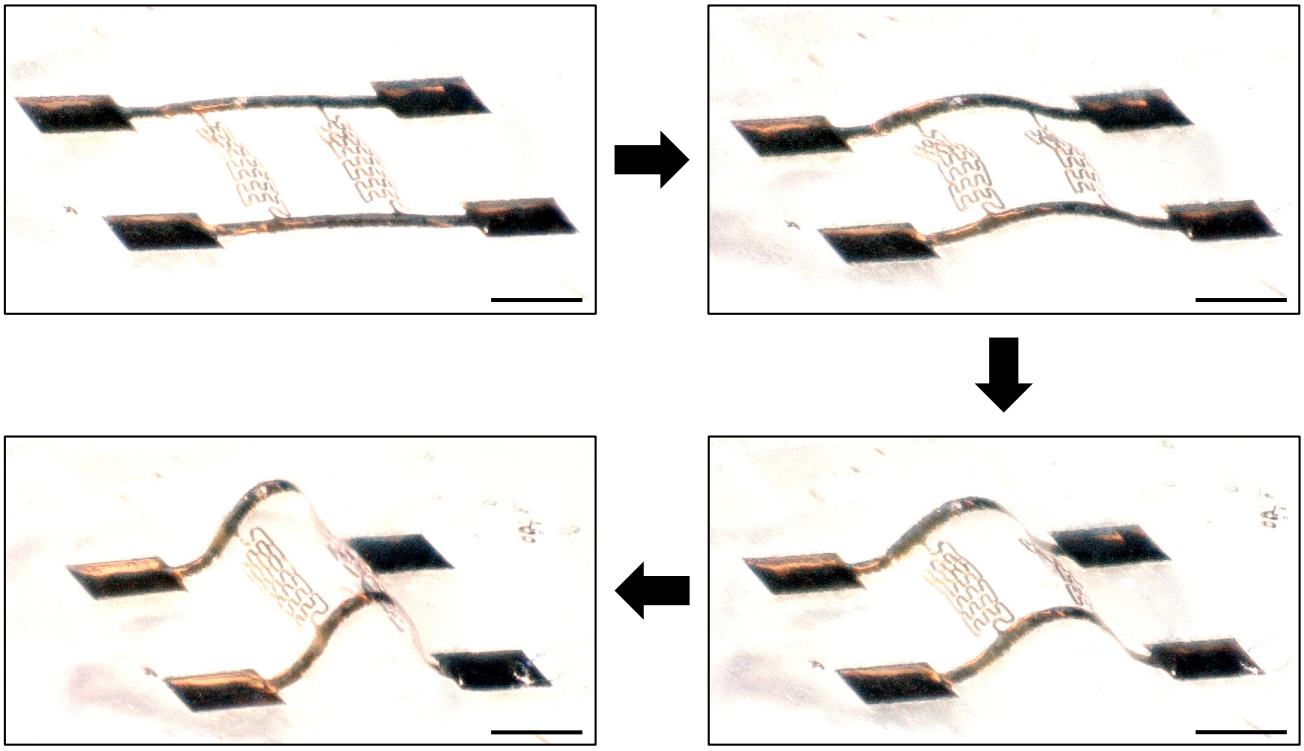

Supplementary Figure 12. Ultra-low-stiffness mesostructure switching between 2D and 3D geometries through stretching and releasing of the elastomer. Scale bars, 500 μm.

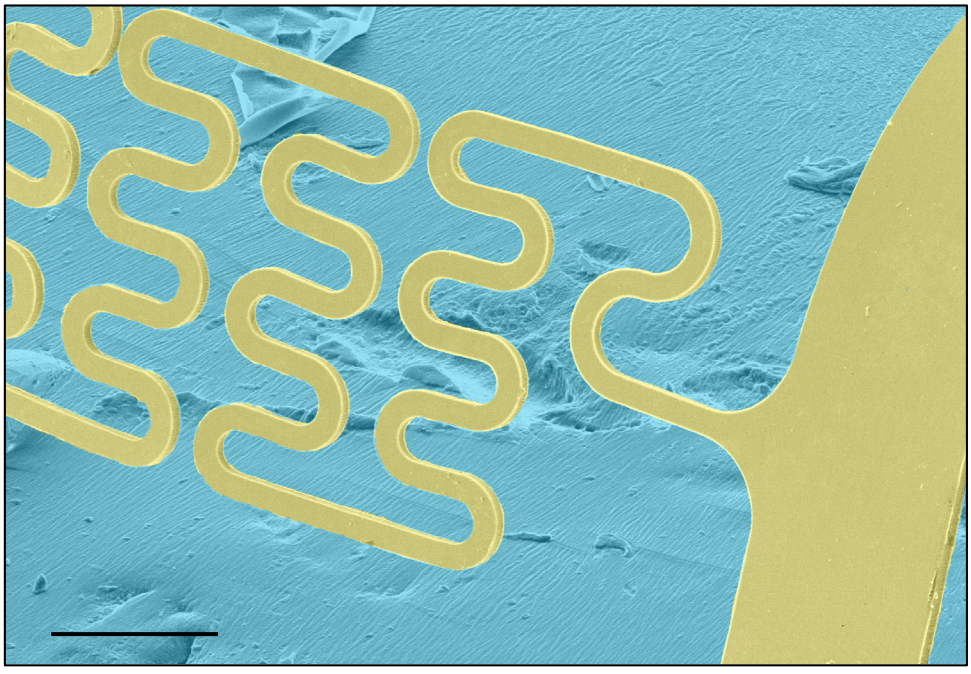

Supplementary Figure 13. Magnified SEM image of the two-order 3D fractal curve. Scale bars, 100 μm.

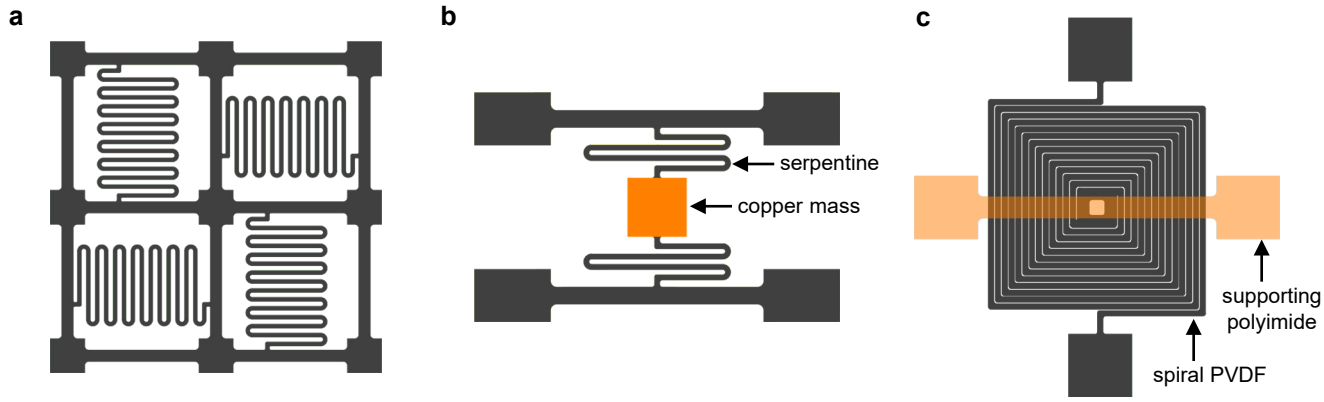

Supplementary Figure 14. 2D layouts of vibration-based energy harvesters. **a,** Array of 3D serpentines. **b,** Bi-stable 3D serpentine with copper mass. **c,** Multilayer 3D spiral structure.

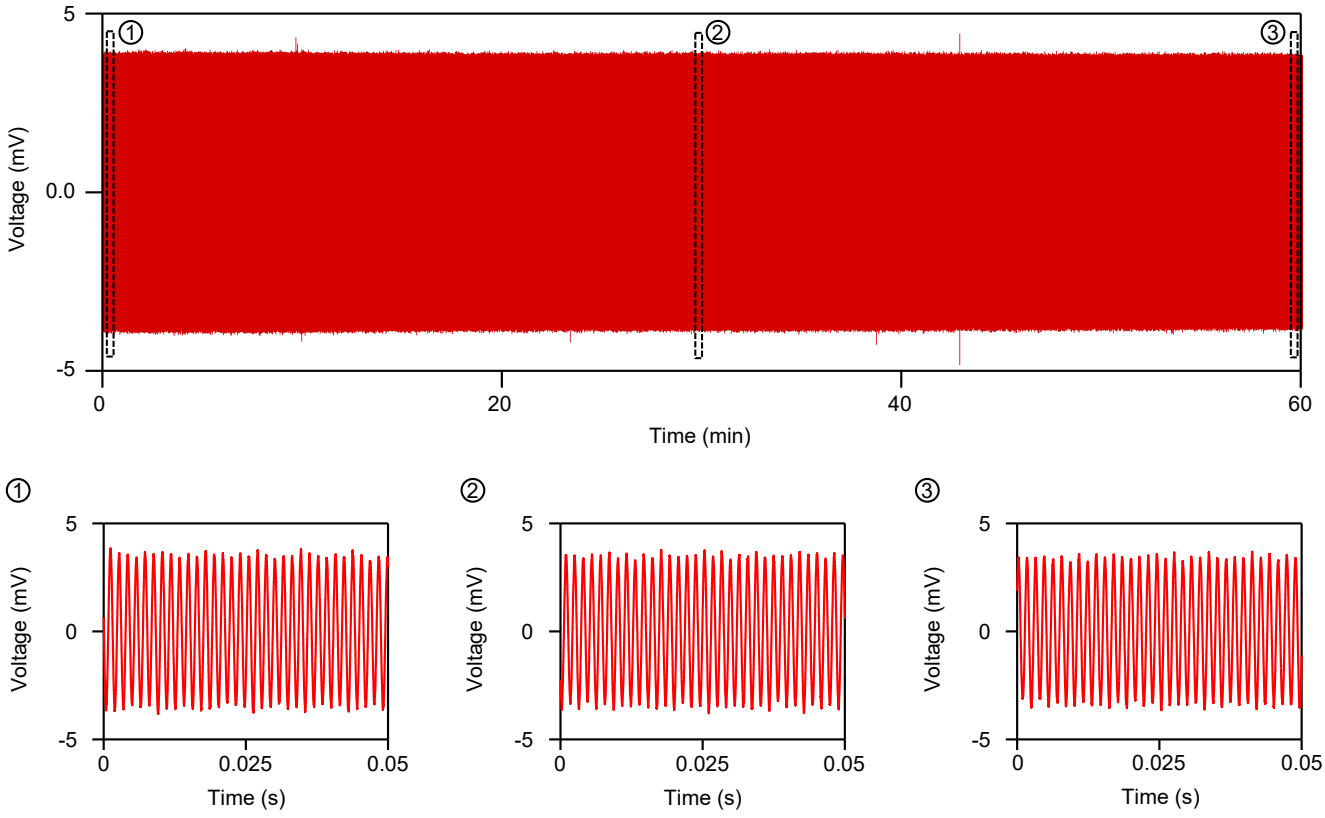

Supplementary Figure 15. Cyclic measurement of the 3D serpentine array under vibration with frequency of 657 Hz and acceleration of 4 *g*.

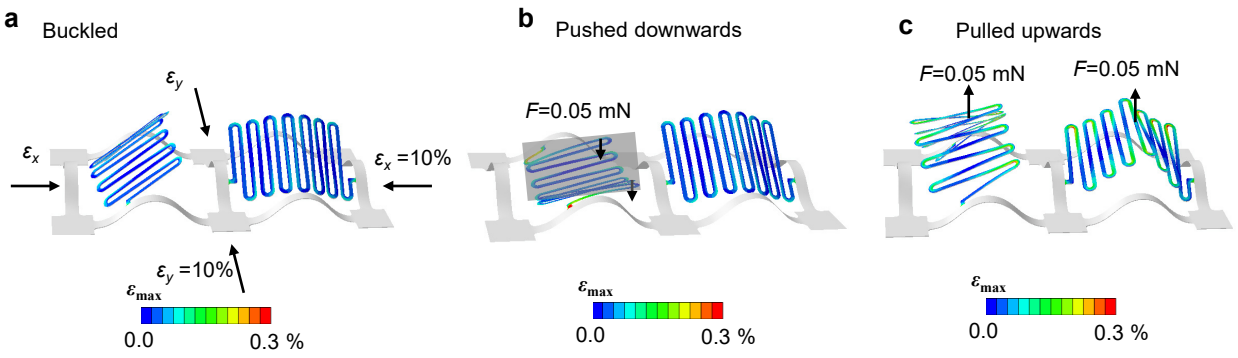

Supplementary Figure 16. Deformation and strain distribution of the 3D vibratory piezoelectric energy harvester (Fig. 2a). a-c, FEA result for the maximum principal strain in serpentine ribbons buckled by 10% compressive strain, pushed downward by a 0.05 mN force and pulled upward by 0.05 mN force, respectively. In (b), the force is applied by pressing with a rigid plate. When the force exceeds 0.05 mN, the serpentine ribbon comes into contact with the underlying substrate.

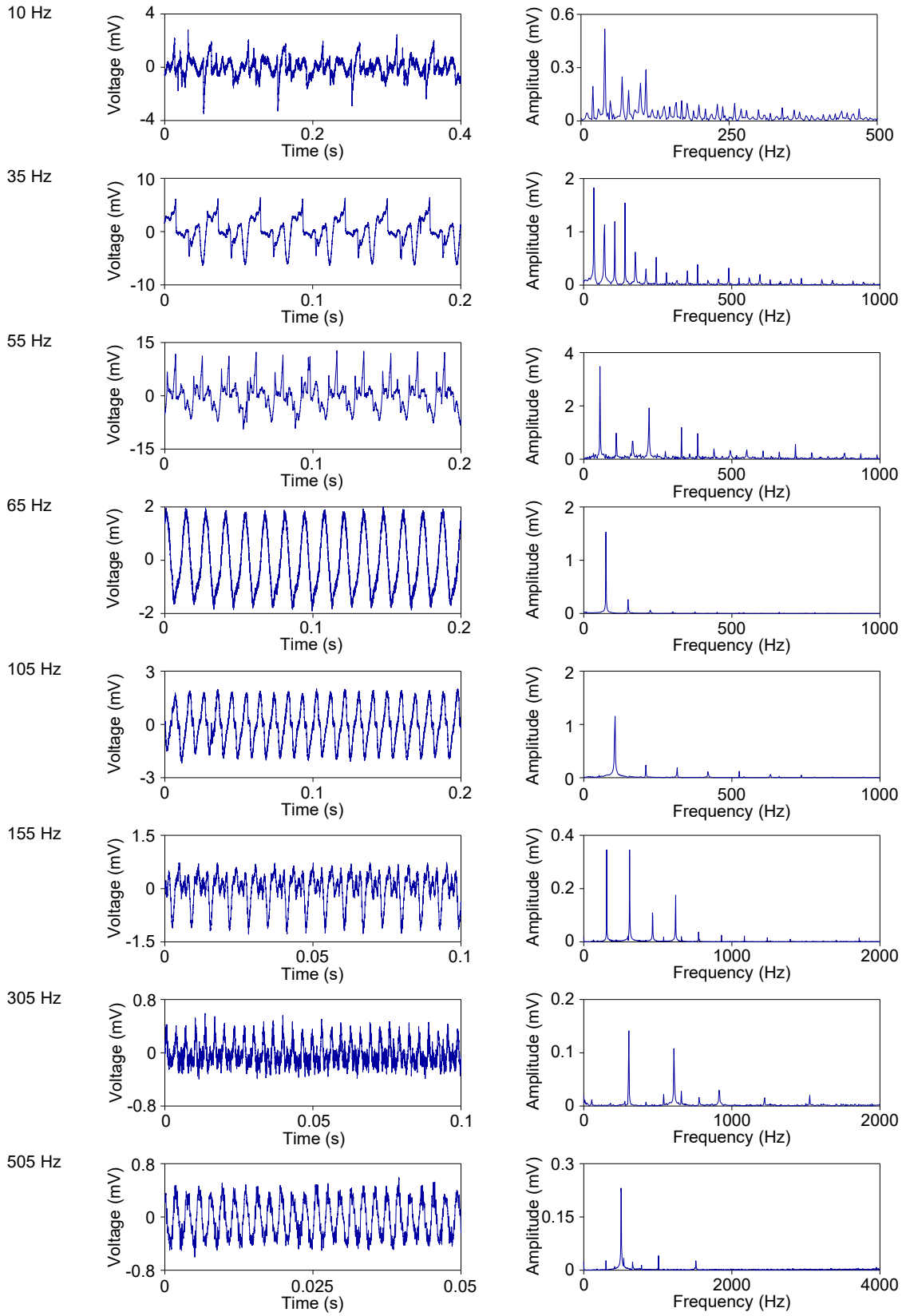

Supplementary Figure 17. Representative time-domain output voltage (left) and corresponding fast Fourier transform (right) of the 3D bi-stable serpentine with copper mass.

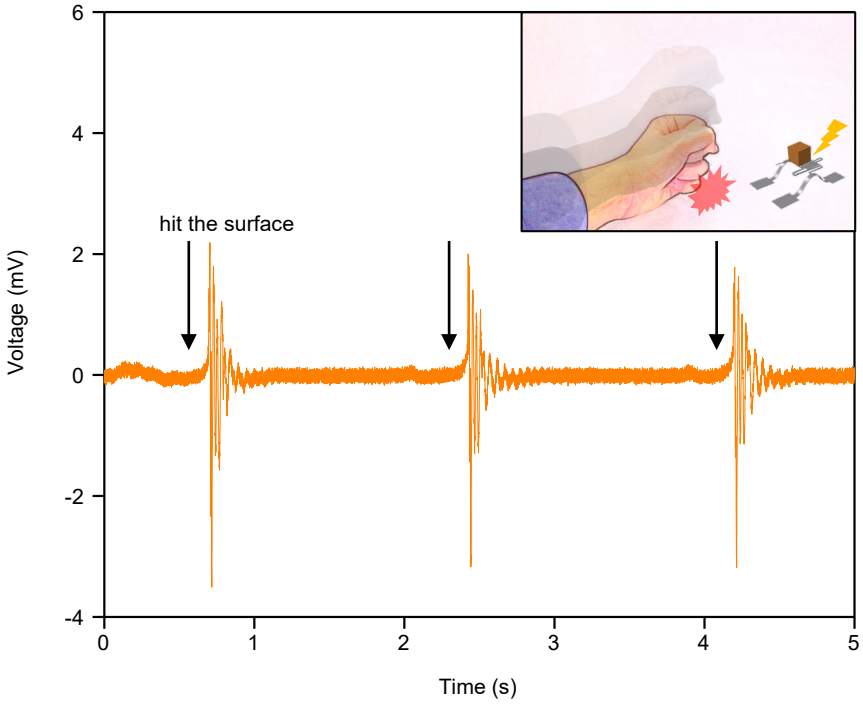

Supplementary Figure 18. Time-domain output voltage of the 3D bi-stable serpentine by periodically hitting the surface at a distance, with an inset that schematically illustrates the testing condition.

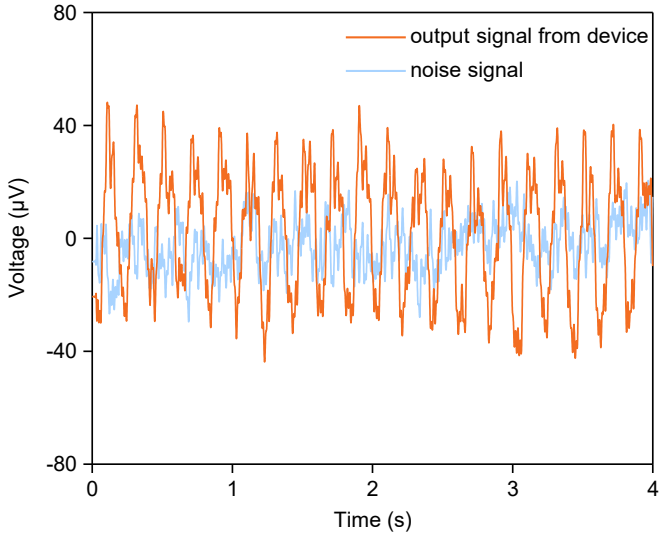

Supplementary Figure 19. Noise signal and output voltage of the bi-stable 3D serpentine structure with a low-pass (20 Hz) filter under vibration (frequency: 5 Hz, acceleration: 0.1 *g*).

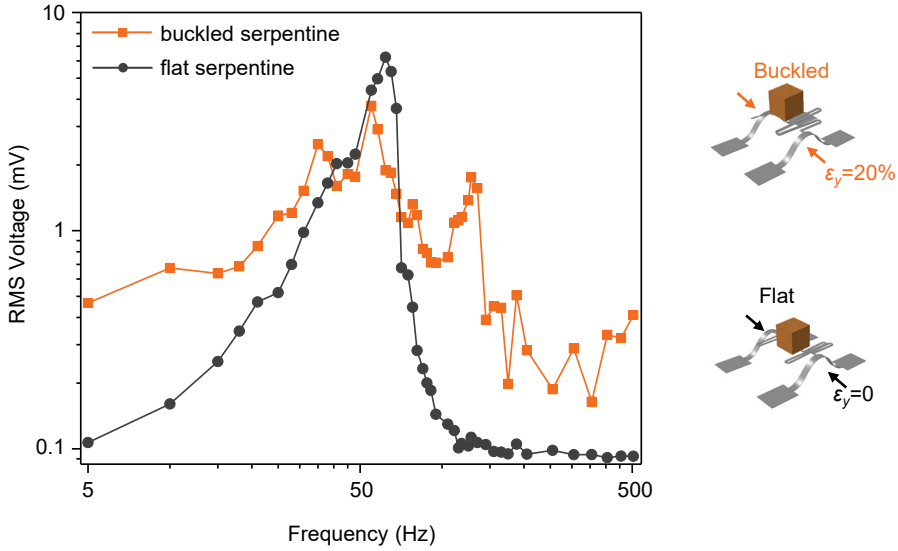

Supplementary Figure 20. RMS voltages of the 3D ultra-low-stiffness mesostructures with bi-stable serpentine and flat serpentine designs.

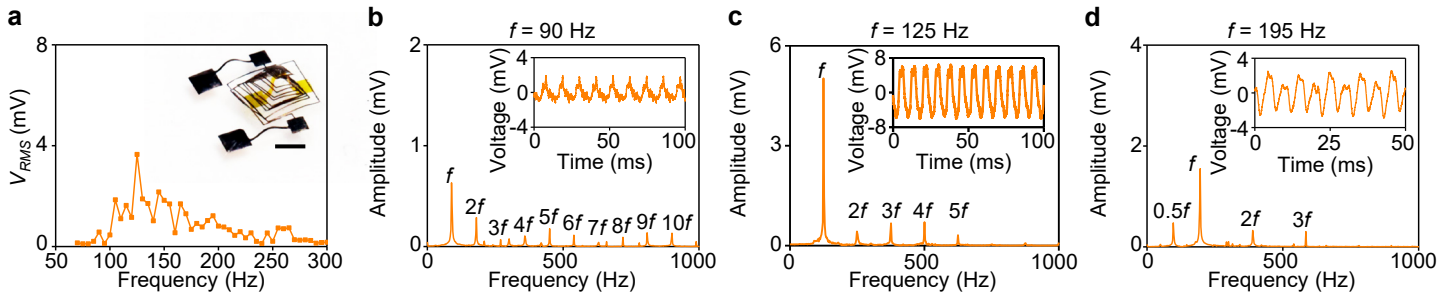

Supplementary Figure 21. Output of the 3D spiral structure. a, RMS voltage under different frequencies. Scale bar, 1 mm. **b-d,** fast Fourier transform at 90, 125 and 195 Hz, with insets show corresponding time-domain output voltage.

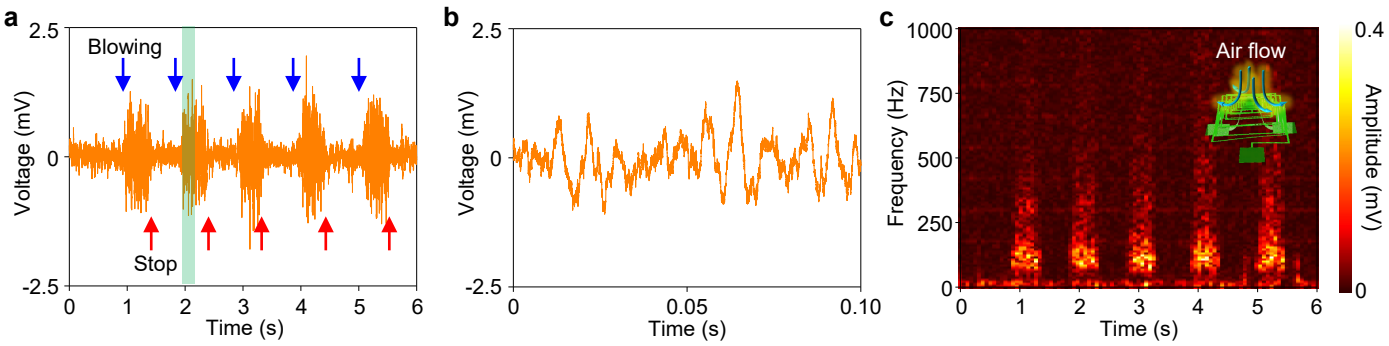

Supplementary Figure 22. Output of the 3D spiral structure from air flow. a, Time-domain output voltage. **b,** Magnified view of the output voltage. **c,** Spectrogram of the data shown in **a**, indicating a wide frequency range from 100 to 200 Hz.

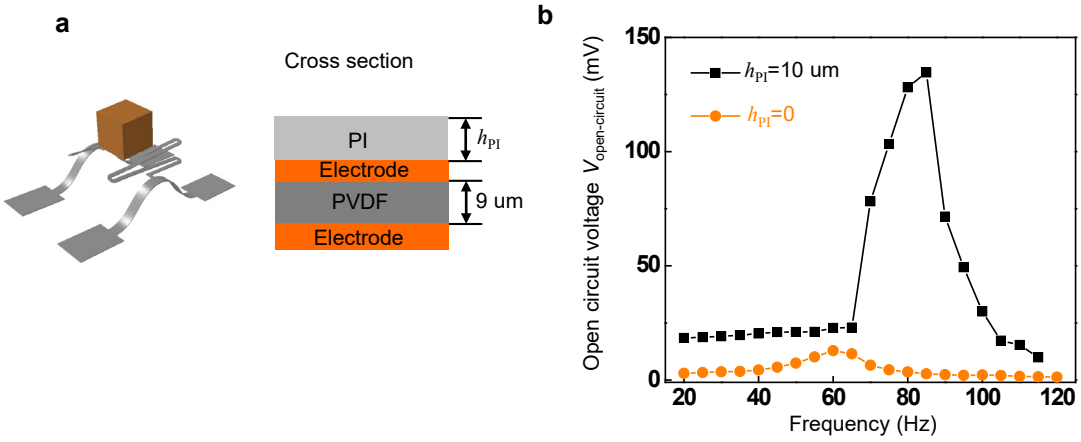

Supplementary Figure 23. Increase the output voltage by the supporting layer that offsets the PVDF from the neutral mechanical plane. a, 3D serpentine structure and its thickness profile. **b**, FEA result of the open-circuit output voltage (RMS).

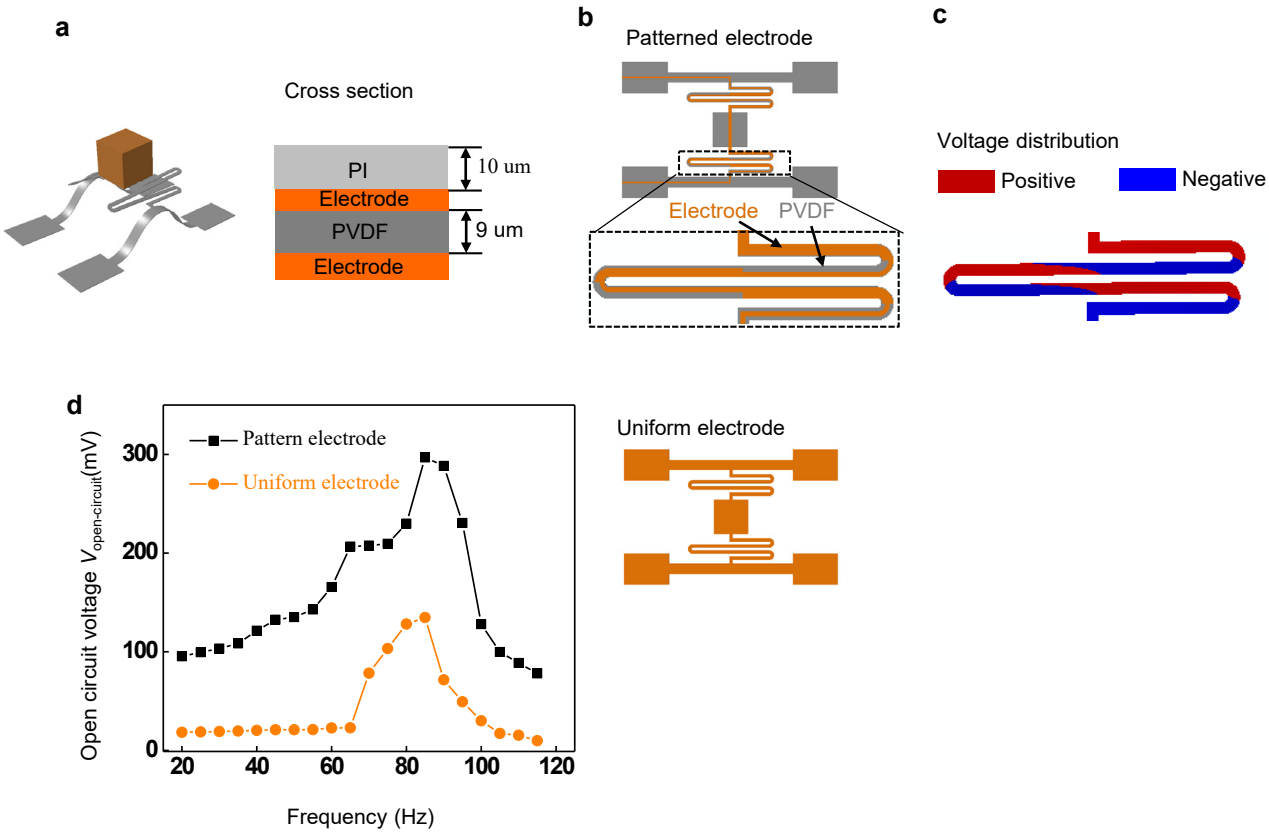

Supplementary Figure 24. Increase the output voltage by the patterned electrode. a, 3D serpentine structure and its thickness profile. **b,** Patterned electrode. **c,** FEA result of the voltage distribution without the electrode. **d,** FEA result of the open-circuit output voltage (RMS).

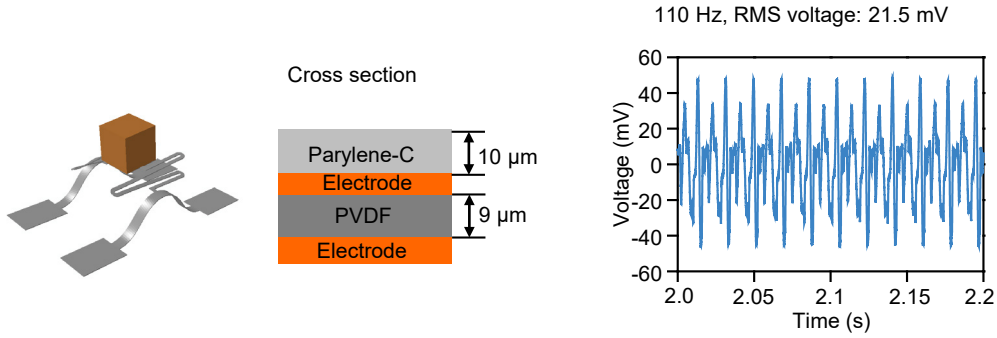

Supplementary Figure 25. Output voltages of the 3D vibratory energy harvester in Fig. 2e with a supporting layer to offset the neutral mechanical plane. At 110 Hz, the RMS voltage is 21.5 mV. In comparison, the largest RMS voltage for the energy harvester without the supporting layer is 4 mV (Fig. 2e) for the frequency in the range of 5-500 Hz.

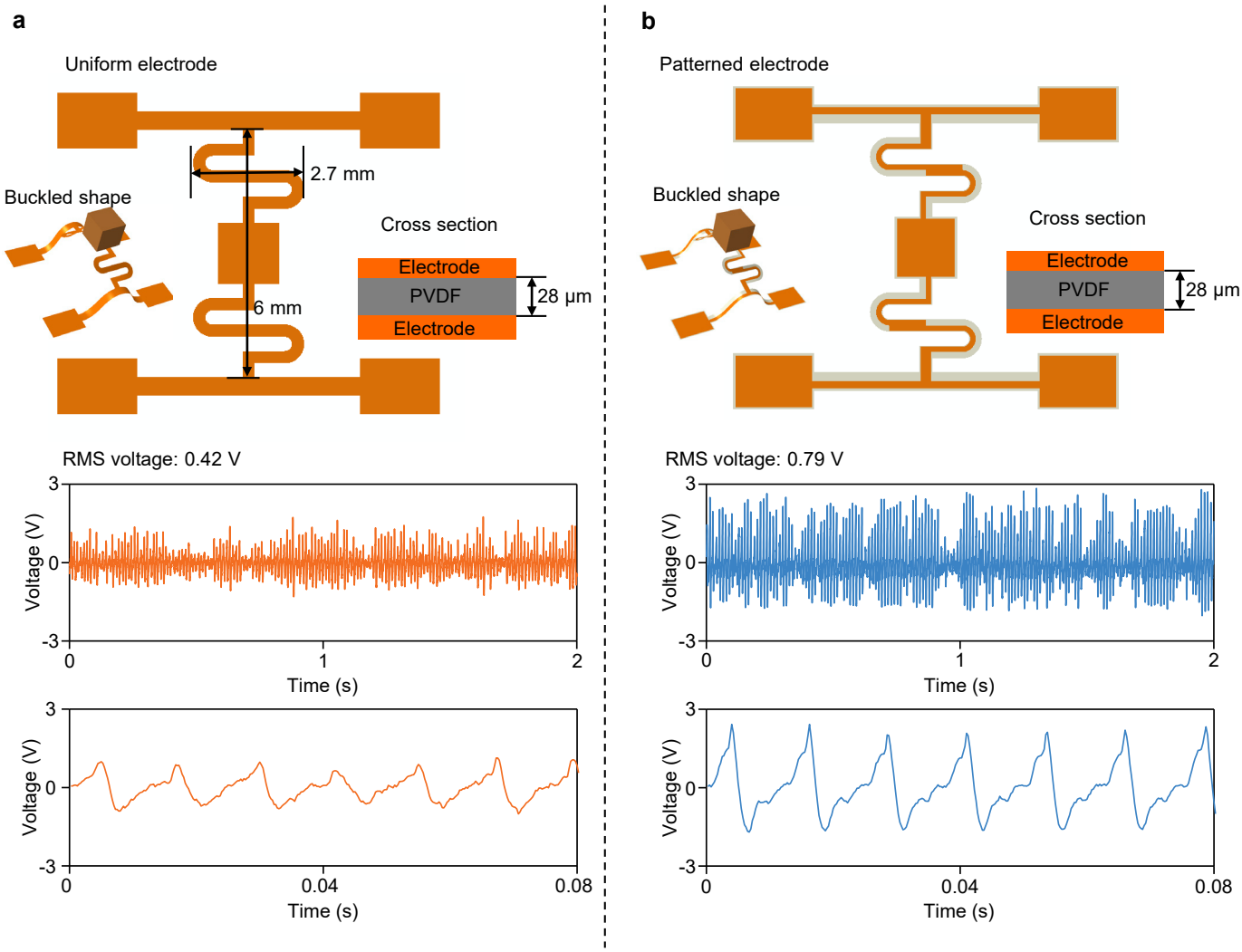

Supplementary Figure 26. Output voltages at 100 MΩ for the 3D serpentine structure during vibration (frequency: 80 Hz, acceleration: 4 *g*) to illustrate the effect of the patterned electrode. Schematic illustrations and output voltages of the structures with uniform electrode (**a**), and patterned electrode (**b**). The intermittent oscillations in the time-domain responses indicate nonlinear vibrations.

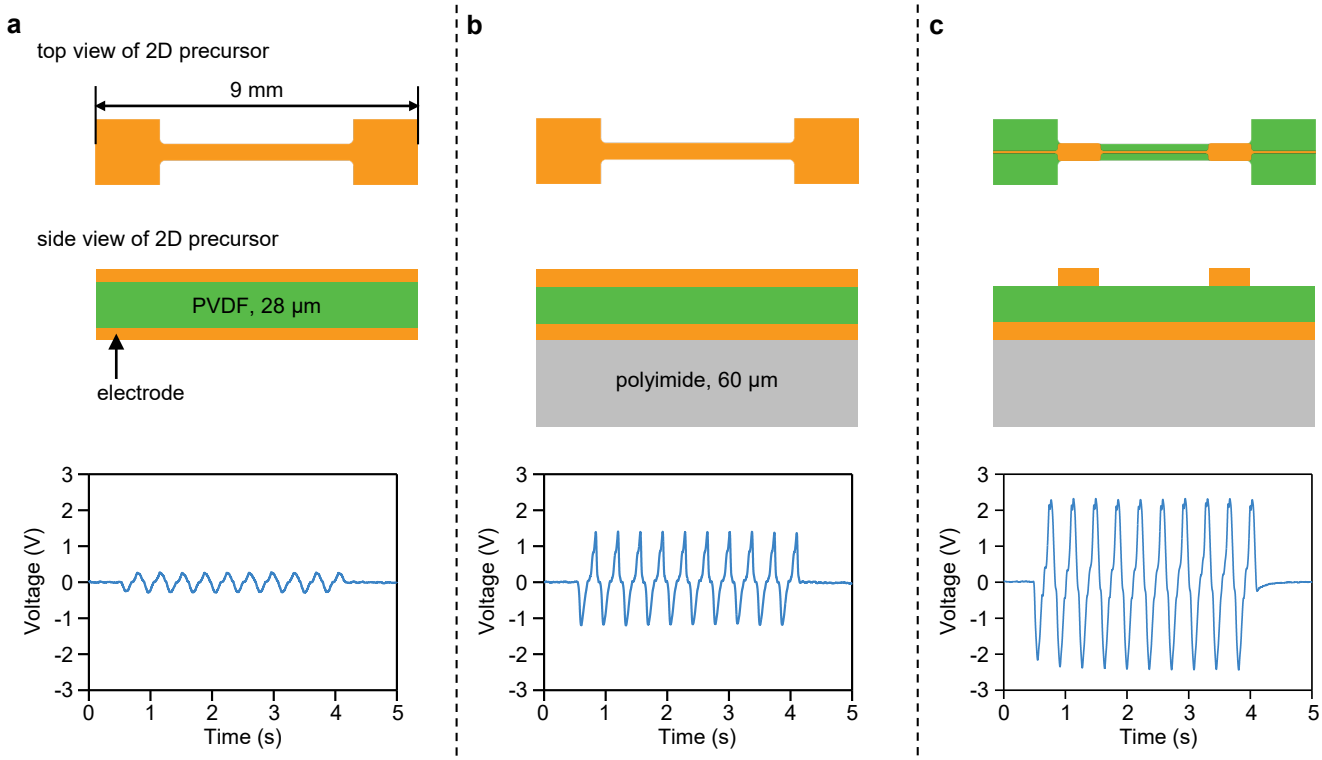

Supplementary Figure 27. Output voltages of 3D piezoelectric ribbons with periodic 10% tensile strain. a, Output voltage of a 3D piezoelectric ribbon. **b,** Output voltage of a 3D piezoelectric ribbon with supporting layer. **c,** Output voltage of a 3D piezoelectric ribbon with supporting layer and patterned electrode.

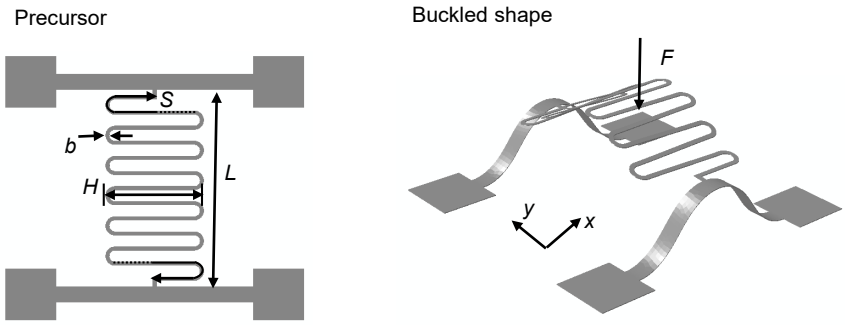

Supplementary Figure 28. Proof-of-concept design of the serpentine pattern with variable geometry parameters for the fundamental study of the broadband and low frequency energy harvester.

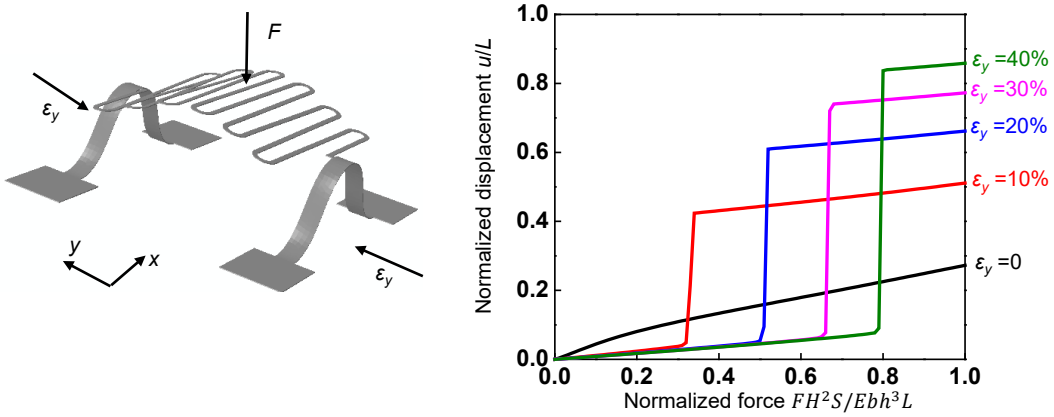

Supplementary Figure 29. Normalized displacement vs. normalized force curve for the serpentine pattern buckled by the compressive strain ranging from 0 to 40%.

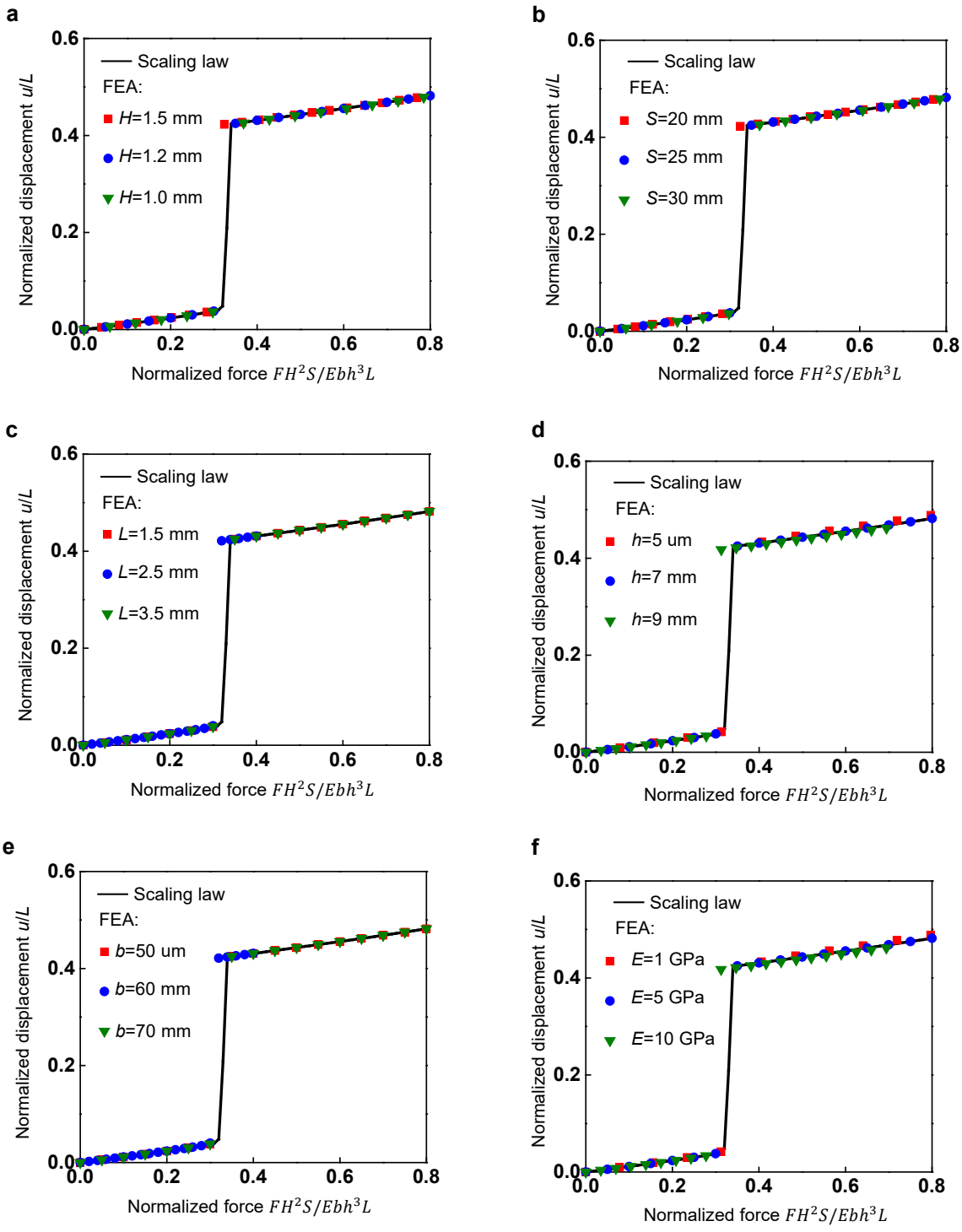

Supplementary Figure 30. FEA validation of the scaling law Eq. (1). The normalized displacement vs. normalized force curve for various **a**, Serpentine height *H*. **b**, Total serpentine arch length. **c**, Serpentine length *L*. **d**, Thickness *h*. **e**, Serpentine width *b*. **f**, Young's modulus *E*.

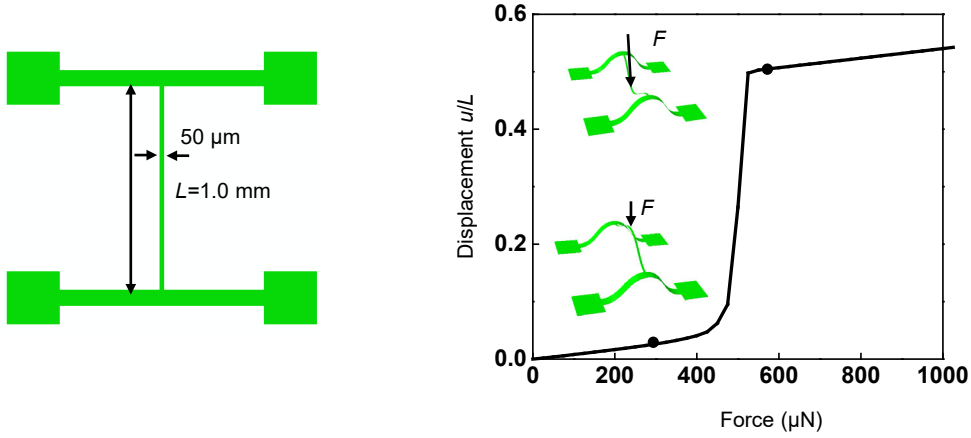

Supplementary Figure 31. The displacement vs. force curve for a straight ribbon. The straight ribbon structure requires 500 μN force to actuate nonlinear deformation. By comparison, a serpentine structure with otherwise similar geometries and materials requires only 2 μN to actuate nonlinear deformation, as the scaling law Eq. (1) (Fig. 2k) suggests.

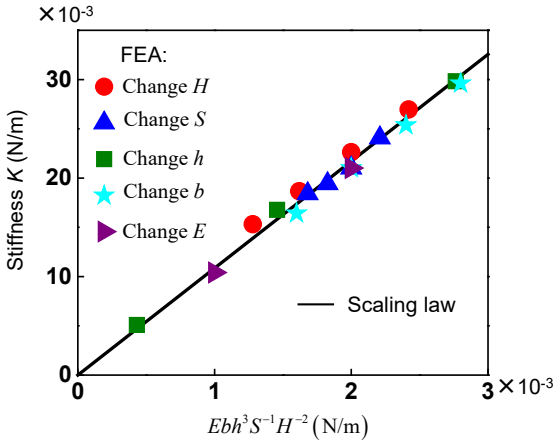

Supplementary Figure 32. FEA validation of the scaling law for serpentine stiffness

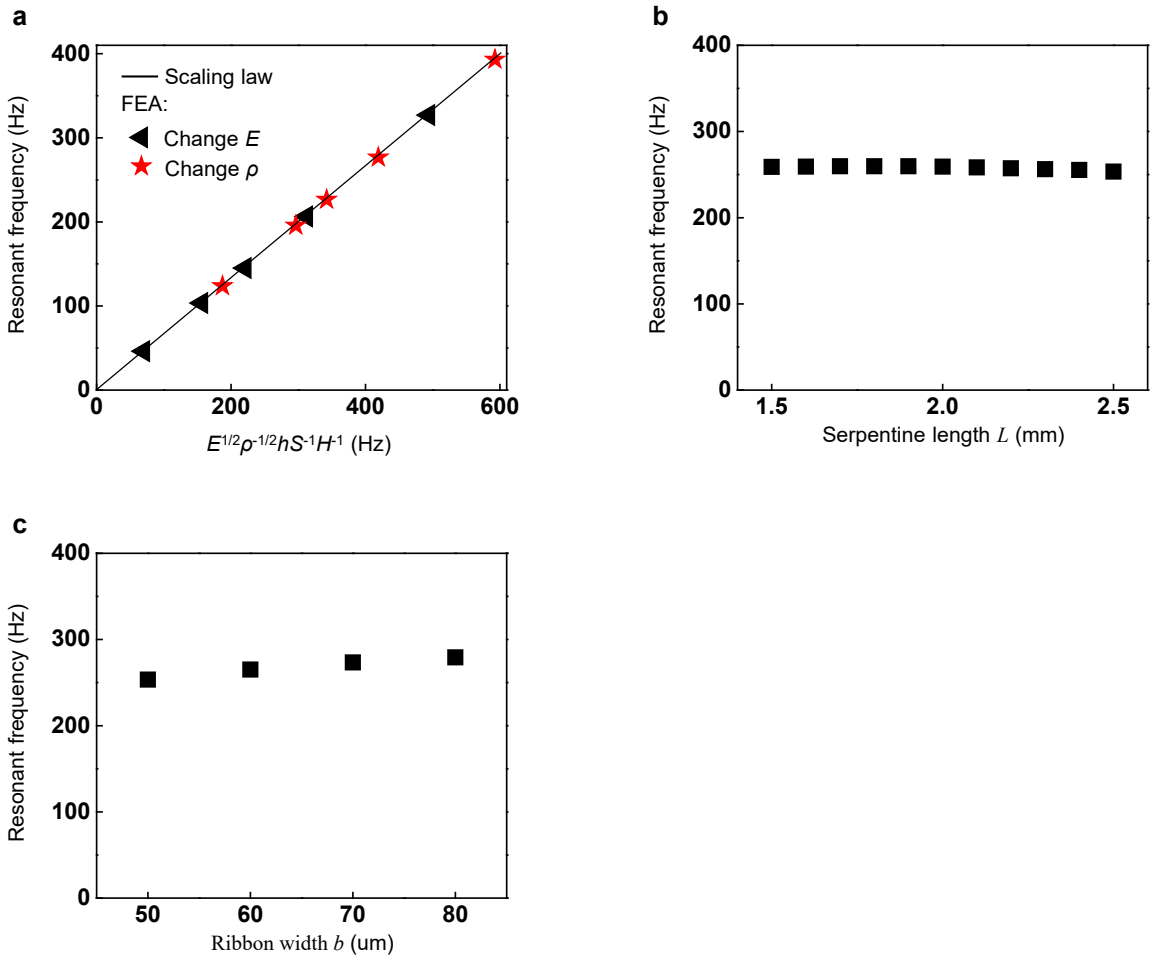

Supplementary Figure 33. FEA result of the variation of the resonant frequency with a, Young's modulus *E* and density *ρ*. **b**, serpentine length *L* and **c**, ribbon width *b*.

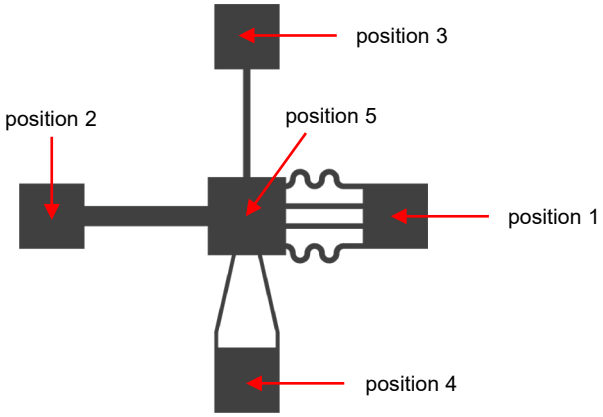

Supplementary Figure 34. 2D layout of impact-based energy harvester.

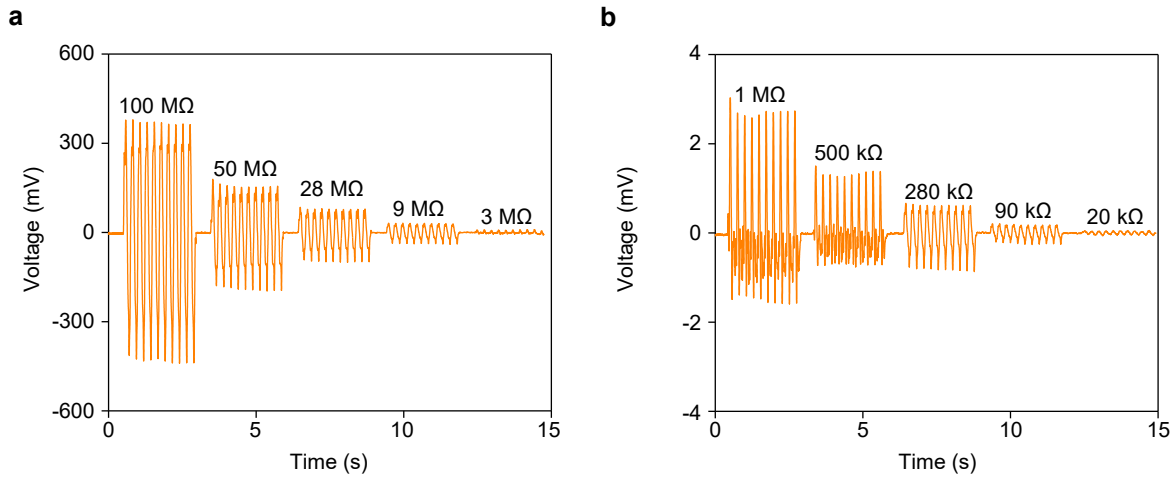

Supplementary Figure 35. Time-domain output voltage of 3D piezoelectric device under different resistances. **a,** Output from 100 MΩ to 3 MΩ. **b,** Output from 1 MΩ to 20 kΩ.

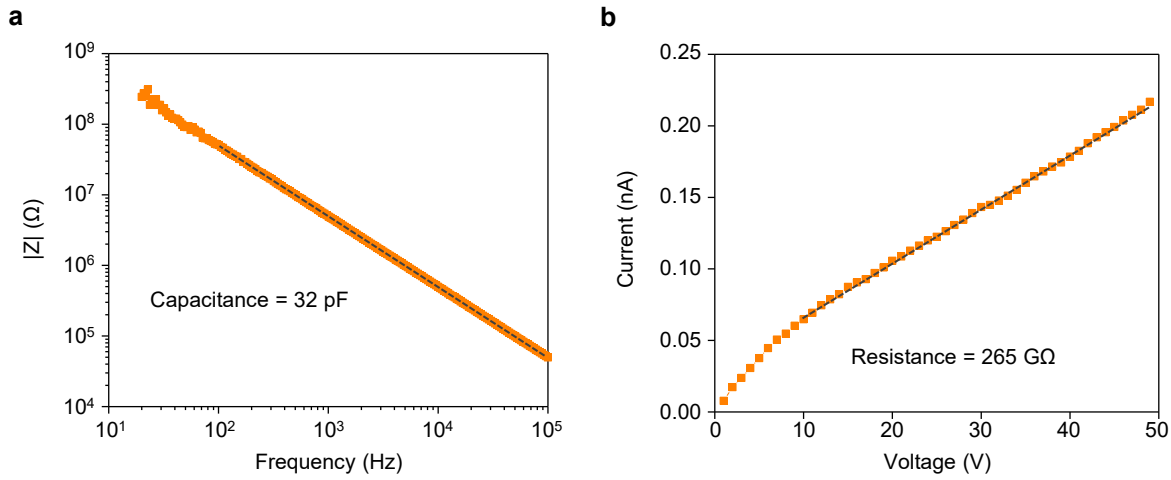

Supplementary Figure 36. Impedance of the 3D piezoelectric device. a, Magnitude of impedance from 20 to 100 kHz, indicating an equivalent capacitance of 32 pF. **b,** I-V curve, indicating an equivalent resistance of 265 GΩ.

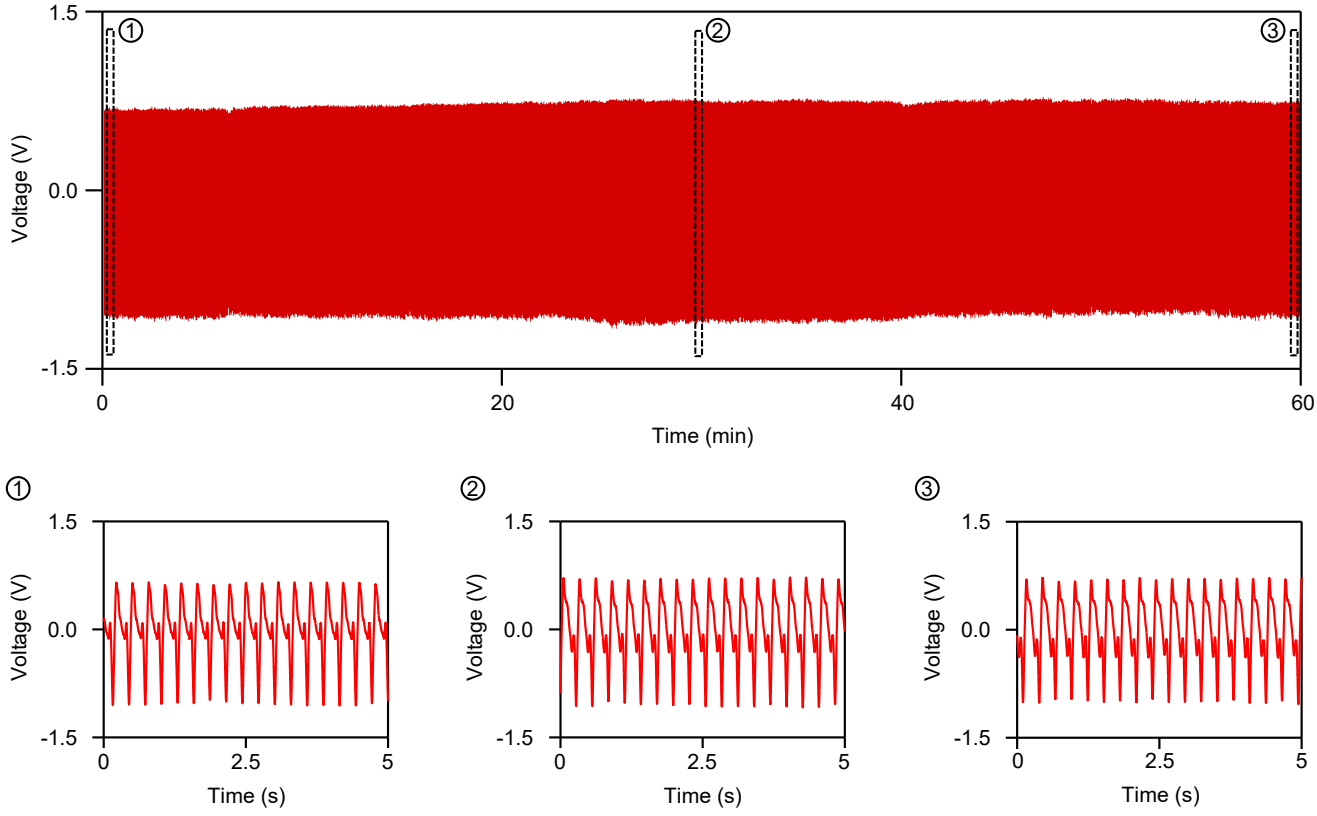

Supplementary Figure 37. Cyclic measurement of the impact-based 3D piezoelectric energy harvester under pressing with normal force of 32 N.

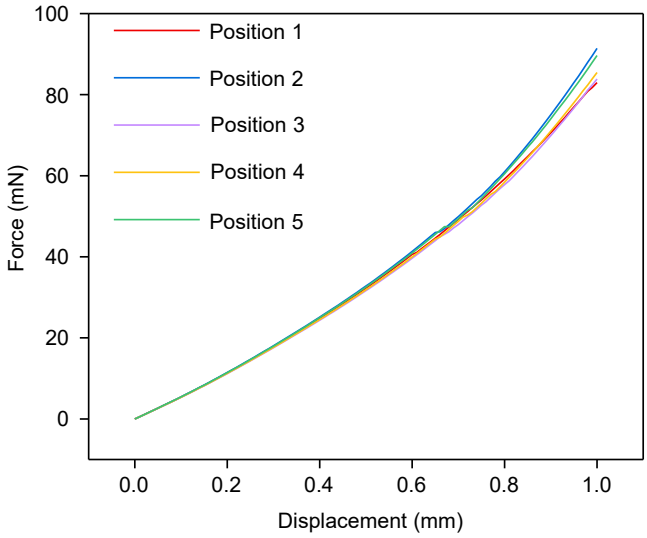

Supplementary Figure 38. FEA results of the relationship of displacement vs. force when applying force on the impact-based 3D piezoelectric device over a circular region with diameter of 0.65 mm.

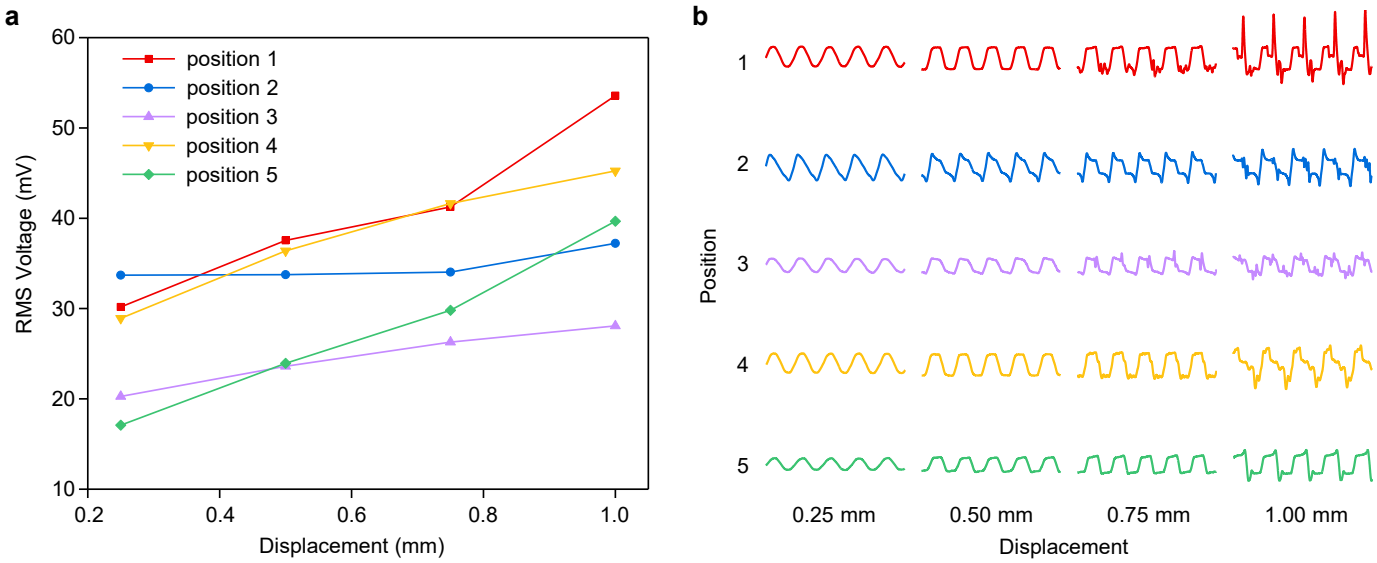

Supplementary Figure 39. Output voltage of the 3D piezoelectric device with external forces applied over different small circular regions. a, RMS voltages at different pressing positions and displacements. **b,** Time-domain response shapes at different pressing positions and displacements.

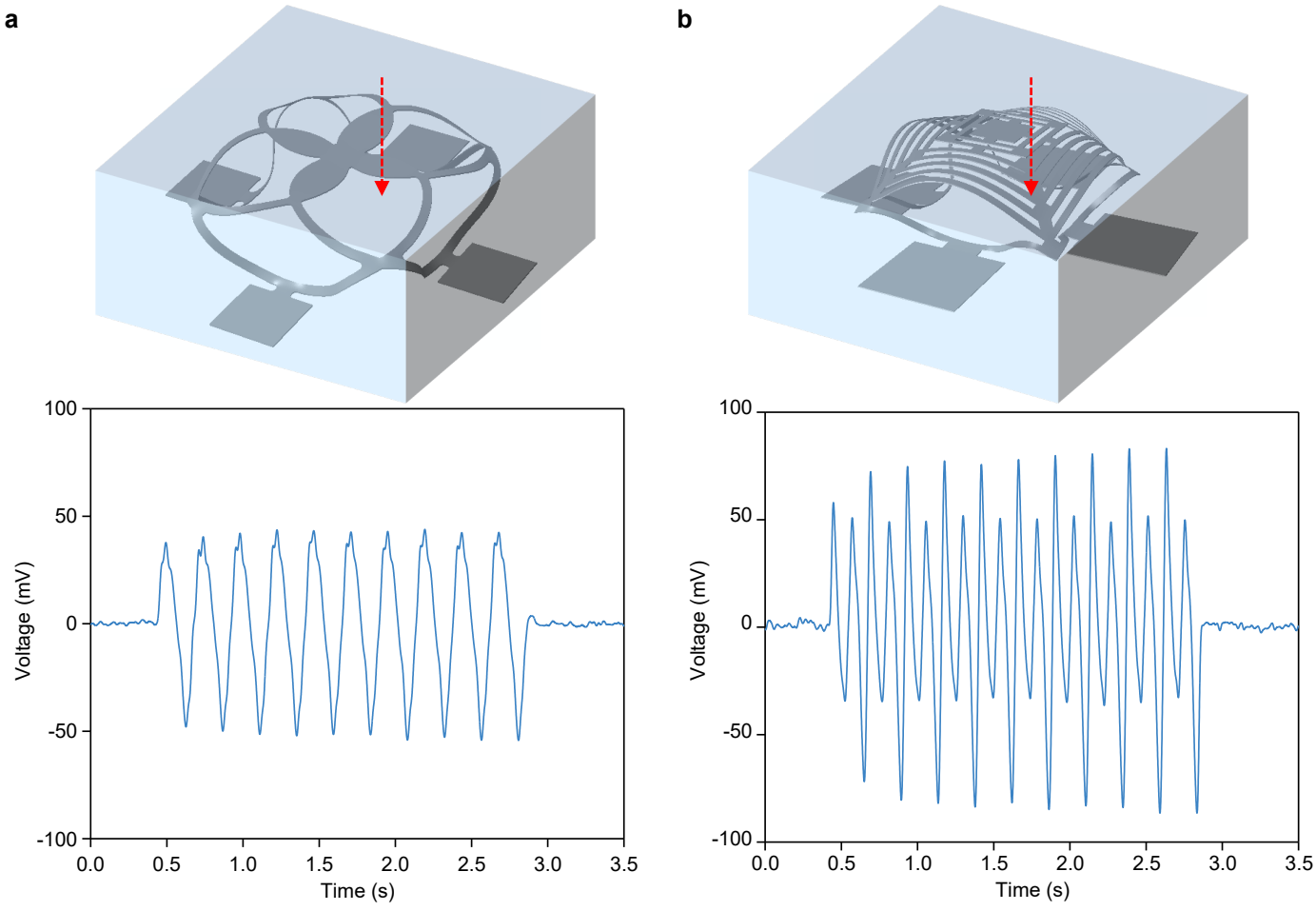

Supplementary Figure 40. Output voltages of different 3D piezoelectric mesostructures with external forces applied over small circular regions (0.65 mm in diameter). a, 3D mesostructure of filamentary components. **b,** 3D mesostructure of mixed membranes and filaments.

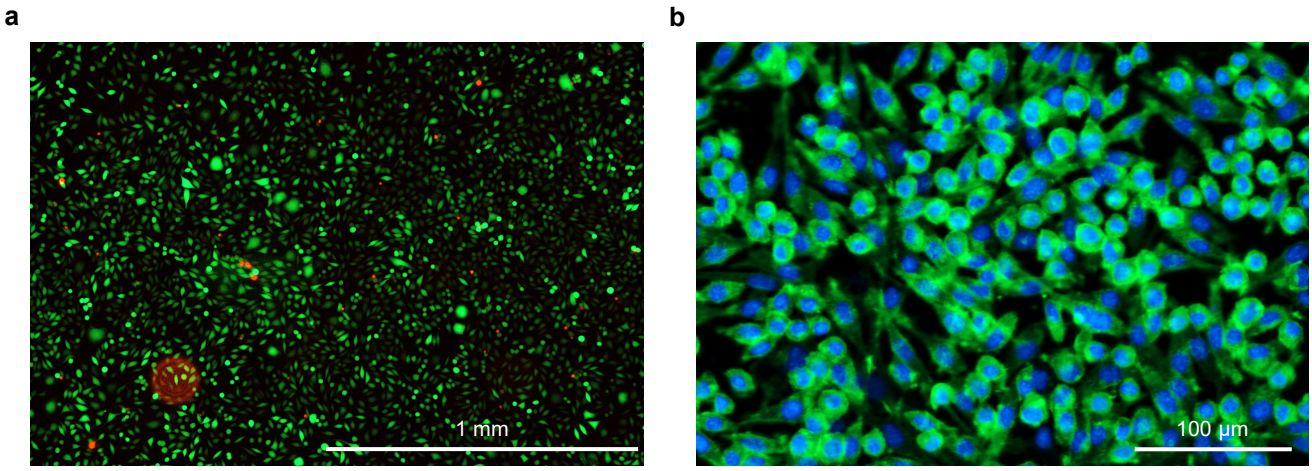

Supplementary Figure 41. Representative fluorescent images of fibroblast cultured on tissue culture plastic. a, Cytotoxicity assay (live/dead test) after 3 days of culturing. Green indicates live cells and red indicates dead cells. **b,** F-actin staining after 7 days of culturing. Green indicates actin filaments and blue indicates cell nuclei.

Supplementary Figure 42. Layout of the 2D precursor for subdermal implantation.

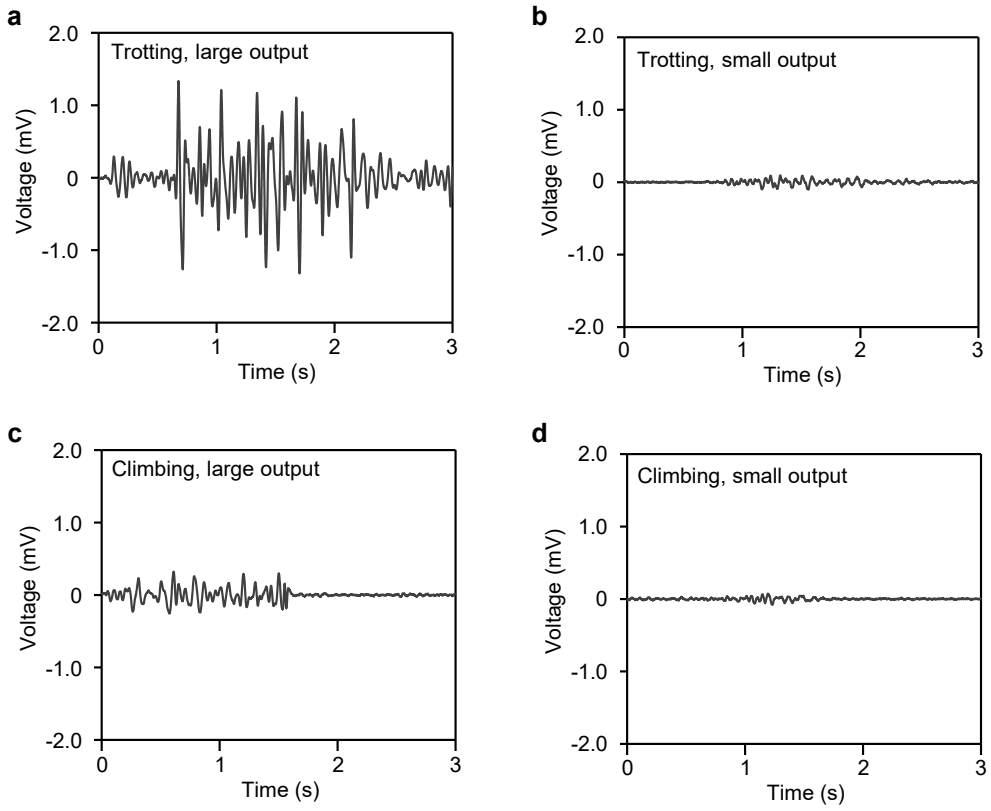

Supplementary Figure 43. Time domain output voltage from the implanted 2D precursor.

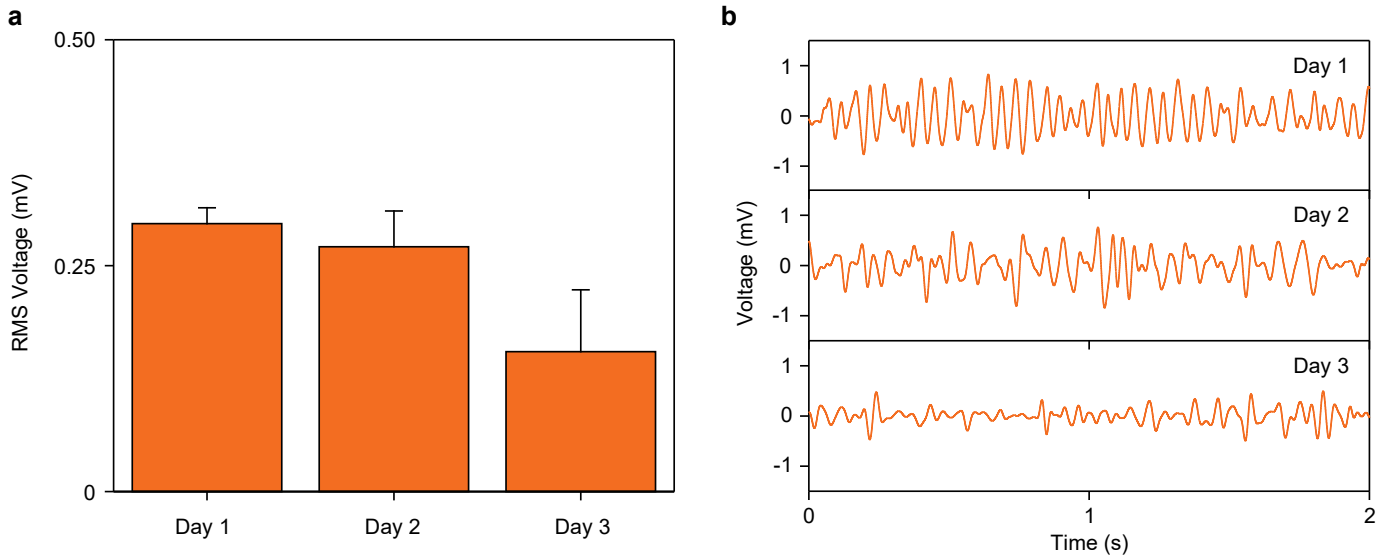

Supplementary Figure 44. Output voltages from the implanted piezoelectric device under trotting behaviors. a, RMS voltages from day 1 to day 3. Data correspond to averages of 5 different trotting behaviors. **b,** Time-domain output voltages from day 1 to day 3.

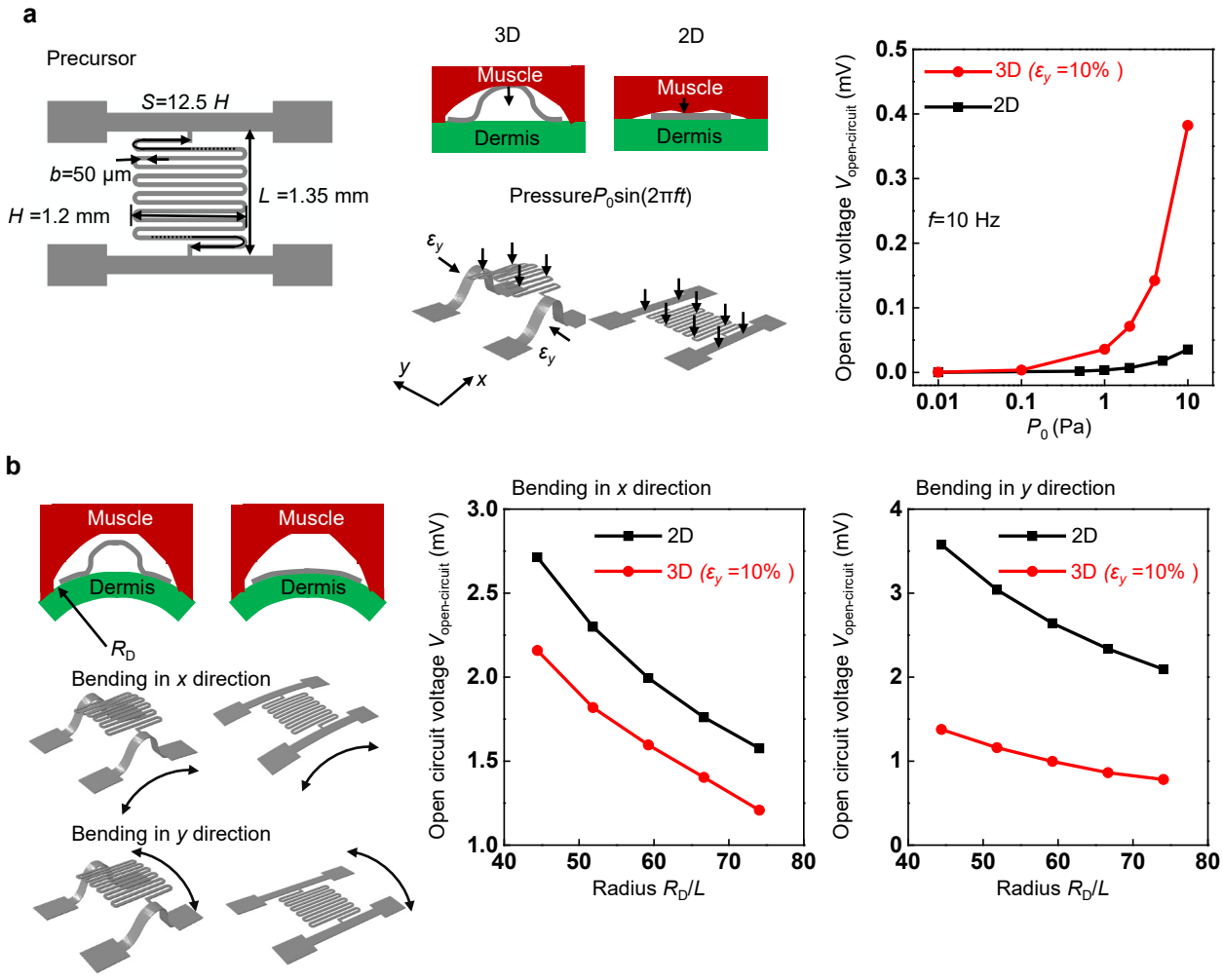

Supplementary Figure 45. a, FEA result of the open-circuit output voltage (RMS) of the 3D structure when the muscle pushes from the top, compared with that of the 2D precursor. Dermis modulus: 100 kPa. **b,** FEA result of the open-circuit output voltage (RMS) of the 3D structure under bending, compared with that of the 2D precursor.

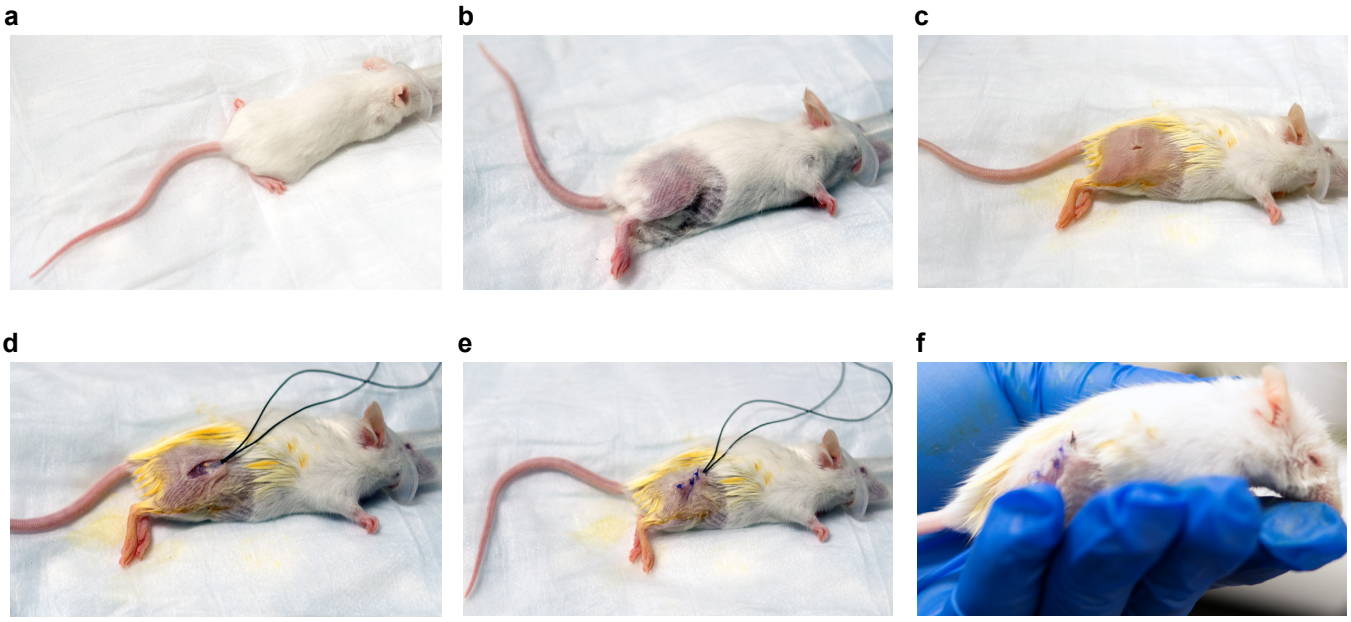

Supplementary Figure 46. Surgical procedure. **a,** Anaesthetizing with isoflurane gas. **b,** Fur removal. **c,** Surgical exposure. **d,** Insertion of a 3D energy harvester into the subcutaneous region. **e,** Suturing and gluing. **f,** Mouse with implanted 3D energy harvester after surgery.